Exploring the potential of Sentinel-3 delay Doppler altimetry for enhanced detection of coastal currents along the Northwest Atlantic shelf

Hui Feng[a b,], Alejandro Egido[b,c,+], Doug Vandemark[a], and John Wilkin[d]*

[a] *University of New Hampshire, Durham, NH, USA*

[b] *Global Science & Technology, Inc., Greenbelt, MD, USA.*

[c] *Laboratory for Satellite Altimetry, College Park, NOAA, MD, USA*

[d] *Rutgers, The State University of New Jersey, New Brunswick, NJ, USA.*

[+] *Now with European Space Agency – European Space Research and Technology Centre, Noordwijk, NL.*

Corresponding author: Hui Feng, hui.feng@unh.edu

Abstract

In this study, we evaluate Sentinel-3A satellite synthetic aperture radar (SAR) altimeter observations along the Northwest Atlantic coast, spanning the Nova Scotian Shelf, Gulf of Maine, and Mid-Atlantic Bight. Comparisons are made of altimeter sea surface height (SSH) measurements from three different altimeter data processing approaches: fully-focused synthetic aperture radar (FFSAR), un-focused SAR (UFSAR), and conventional low-resolution mode (LRM). Results show that fully-focused SAR data always outperform LRM data and are comparable or slightly better than the nominal un-focused SAR product. SSH measurement noise in both SAR-mode datasets is significantly reduced compared to LRM. FFSAR SSH 20-Hz noise levels, derived from 80-Hz FFSAR data, are lower than 20-Hz UFSAR SSH with 25% noise reduction offshore of 5 km, and 55-70% within 5 km of the coast. The offshore noise improvement is most likely due to the higher native along-track data posting rate (80 Hz for FFSAR, and 20 Hz for UFSAR), while the large coastal improvement indicates an apparent FFSAR data processing advantage approaching the coastlines. FFSAR-derived geostrophic ocean current estimates exhibit the lowest bias and noise when compared to *in situ* buoy-measured currents. Assessment at short spatial scales of 5-20 km reveals that Sentinel-3A SAR data provide sharper and more realistic measurement of small-scale sea surface slopes associated with expected nearshore coastal currents and small-scale gyre features that are much less well resolved in conventional altimetric LRM data.

Keywords: Delay-Doppler and synthetic aperture radar altimetry; Sentinel-3; Sea surface height (SSH); Geostrophic current.

1. Introduction

Delay Doppler Altimetry (DDA), also called Synthetic Aperture Radar (SAR) altimetry (Raney et al., 1998, 2012), is a relatively new ocean and ice radar altimeter technique that differs from conventional pulse-limited radar altimetry (PLRA) used by ocean observing satellites such as TOPEX/Poseidon and Jason-1, -2, and -3. In PLRA, pulses are transmitted and received continuously, and surface return echoes are processed incoherently on a pulse-by-pulse basis (Fu and Cazenave, 2001). In a DDA/SAR closed-burst mode altimeter, the pulses are transmitted and received in bursts with a much higher pulse repetition frequency so that successive pulses within a burst are highly correlated. The received pulses then contain additional inter-pulse Doppler phase information. Ideally, the Doppler frequency bandwidth can fully exploit the return power and phase to improve data precision using specifically designed data post-processing approaches. The DDA/SAR technique coherently combines the echoes from a target during its entire illumination time, synthesizing an antenna aperture that has an effective scale of several km. As a result, DDA/SAR altimetry can provide the along-track higher resolution, an order of magnitude finer than PLRA, theoretically capable of reaching to half of the physical antenna diameter (0.5 m).

One expected beneficiary of DDA/SAR systems is the study of coastal ocean circulation applications, where observations of short spatial scales are of paramount interest. Presently, the CryoSat-2 SIRAL (Synthetic Aperture Interferometric Radar Altimeter), Sentinel-3 SRAL (Synthetic Aperture Radar Altimeter), and Sentinel-6/Michael Freilich satellite altimeters all provide SAR-mode and PLRA-equivalent Low-Resolution Mode (LRM) datasets to allow evaluation of this new type of altimeter sea level measurement for coastal ocean sea level studies.

Several signal processing approaches have been proposed and applied to analyze SAR-mode data. On one hand, the standard or nominal Un-Focused SAR (UFSAR) processing greatly improves on LRM data by lowering range measurement noise and resolving features to within a few hundred meters from the coast, but without a full consideration of the inter-pulse phase signals **(**Raney et al., 1998; Martin-Puig and Ruffini, 2009; Ray et al., 2015). This next, more intensive level of post-processing, the Fully-Focused SAR (FFSAR) method, has been proposed to further improve data for fine-scale oceanic and coastal applications (Raney et al., 2012; Egido and Smith, 2017; Guccione et al., 2018). In FFSAR, the different bursts within the integration aperture are coherently processed using phase compensation to improve the along-track resolution up to its theoretical spatial limit.

Recent studies have demonstrated the advantages of SAR mode in comparison with LRM. For instance, CryoSat-2 UFSAR data exhibit lower noise versus LRM data in the coastal ocean (Fenoglio-Marc et al., 2015; Cipollini et al., 2017; Dinardo et al., 2018). Furthermore, CryoSat-2 FFSAR data outperformed both UFSAR and LRM results in the open ocean (Egido and Smith, 2017) and on the coastal Nova Scotia Shelf (NSS) (Feng et al., 2018a). However, the uneven time-space availability of CryoSat-2 SAR altimeter observations in the NSS region limited the scope and conclusions drawn in the latter study. The present study seeks to use Sentinel-3 (S-3) SAR mode datasets and their improved and regular time and spatial coverage along the Northwest Atlantic (NWA) shelf to provide a more comprehensive evaluation of the potential benefits of SAR altimetry in this region. One question is whether these finer-scale altimeter data products can better resolve coastal current and small-scale sea surface height signatures along the NWA shelf, following on from recent altimeter-based investigations of regional circulation dynamics (Feng et al., 2011, 2016, 2018b; Grodsky et al., 2018a, 2018b, 2021).

An overall project goal is to enhance regional coastal oceanographic studies by providing the best available altimeter measurements of sea surface height (SSH) and SSH-derived geostrophic current (*Vg*) in the NWA coastal zone. This goal is achieved by investigating how well Sentinel-3 SAR (FFSAR and UFSAR) data performs with respect to conventional LRM measurements. Specific objectives are (i) to quantify SSH data quality near the coast, (ii) to estimate noise in the altimeter-derived SSH and SSH-derived *Vg* estimates, across the shelf and up to the coastline, (iii) to determine if SAR mode data are better able to resolve coastal currents and fine-scale SSH signals like small-scale gyres, and (iv) to explore objective length scales needed to infer across-track geostrophic currents that closely align with the along-shelf current over much of this region.

The paper is laid out as follows. Section 2 briefly introduces the study region and recent altimeter-related studies that motivate this work. Section 3 describes the datasets and analysis method, including how the geophysical parameters SSH and SSH-inferred *Vg* are estimated and assessed in a coastal context. Results and discussions are presented in Section 4. A summary is provided in Section 5.

2. Study region and recent altimeter data applications

2.1. General oceanography in the region

Along the NW Atlantic coastal shelf, a southwestward shelf flow predominates, originating from the Labrador Sea and Grand Banks, moving along the Nova Scotian Shelf (NSS) towards the Mid-Atlantic Bight (MAB) and Cape Hatteras. This flow is sustained by a large–scale alongshore pressure gradient (Csanady, 1978; Lentz 2008). Smaller inner-shelf scale current features appear especially inside the Gulf of Maine (GoM) and along the NSS where complex submarine bathymetric features interact with the tides to generate persistent small-scale circulation patterns. Conventional LRM satellite altimetry is unable to resolve many of these features (Feng et al., 2011, 2018).

Circulation on the western Scotian shelf includes a shelf-scale southwest flow and local bathymetry-induced currents. An inner-shelf flow known as the NSS Current is sourced from the Newfoundland Shelf and the Gulf of St. Lawrence and an offshore branch is an extension of the Labrador Current along the shelf edge. Well-studied inner-scale circulations exist including clockwise gyres on Browns and Sable Island Banks, and a partial counterclockwise gyre around Emerald Basin, each varying seasonally (Smith, 1989; Loder et al., 2003; Hannah et al., 2001; Shan et al., 2016**).**

The mean circulation of the GoM is cyclonic, and its variation is controlled by Nova Scotian Shelf inflow, by local freshwater runoff, and wind forcing that includes the contributions from local and remote wind forcing outside of the domain under consideration. Its heterogeneous offshore bathymetry forms a self-contained oceanic system. Generally, Georges and Browns Banks and Nantucket Shoals greatly restrict the water mass exchange between the GoM and NWA shelf, limiting this exchange principally to three deep channels: the Northeast Channel, the North Channel near southwestern Nova Scotian Shelf, and the Great South channel (Fig. 1a). The Maine

Coastal Current (MCC) inside the Gulf is an extension of the NSS Current and continues along the Maine coastal shelf to Cape Cod, and on to the MAB shelf. On its way, the MCC passes the mouth of the Bay of Fundy, and turns along the eastern GoM coast. The eastern component of the MCC is often directed offshore to the central GoM as a plume-like feature of colder water. A portion of the offshore plume is entrained to form a cyclonic gyre over Jordan Basin, and the remaining portion continues toward the western GoM, called the Western MCC. Many previous studies have shown that the water mass exchange in the deep channels and MCC can vary sub-tidally, seasonally, and inter-annually using both observations (Brown and Irish, 1993; Pettigrew et al., 2005; Geyer et al., 2004; Townsend et al., 2015; Smith et al., 2001) and models (Urrego-Blanco and Sheng, 2014; Brickman et al., 2016; Katavouta et al., 2016). The fact that circulation variation on these NWA shelves occurs over a wide spectrum of time and space scales creates challenges for regional monitoring and prediction.

2.2. Previous regional altimeter studies

Satellite altimetry now provides routine ocean surface topographic observations that continue to significantly advance global understanding of ocean circulation dynamics.

Satellite altimetry data products become more valuable for providing essential information on ocean surface currents for various applications, particularly in the shelf and coastal regions (Liu et al., 2014; Wilkin et al., 2018). But it is well recognized that conventional altimeter data utility and quality degrades in coastal regions for several reasons. Dedicated community efforts (Vignudelli et al., 2011) have attempted to improve the quality of coastal altimeter data by improving needed geophysical range corrections, advancing mean dynamic topography (MDT) estimates, and objectively merging multiple-mission altimeter data for space/time resolution improvements. While remarkable improvements have been made, several fundamental measurement limitations remain.

Altimeter data applied to NW Atlantic studies has included investigations into circulation structures and variations on the deeper Scotian shelf-slope ocean (Han et al., 2002; 2007). Recently, we demonstrated that the along-shelf geostrophic currents inferred from altimeters (TOPEX, Jason-1 and Jason-2) on the southwest NSS provide new perspectives on the NSS shelf transport variability, a critical flow that modulates sub-surface GoM coastal transport (Feng et al., 2016). That finding indicates that the long-term altimeter observations offer dynamic information with the potential to support hydrographic monitoring and regional circulation prediction inside the GoM. In parallel, significant progress has been made in data assimilation of altimeter-measured sea surface height into a regional numerical circulation forecast model for the NSS-GoM-MAB shelf region (Wilkin et al., 2018; Levin et al., 2018), and in evaluating the impact these data have on ocean state estimates (Levin et al. 2021)

Objective documentation of altimeter measurement data quality is one important factor influencing potentially wider usage by coastal oceanographers. Our studies have used *in situ* current and sea level measurements to quantify both strengths and limitations of altimeter-derived geostrophic currents across the region (Feng et al., 2011, 2016, 2018b).

Gridded daily upper ocean current data products, such as GlobCurrent (Rio et al., 2014), which merge data from multiple satellite altimeters, have also recently become available. These products provide an altimeter-inferred absolute geostrophic current estimate augmented by a surface Ekman-layer estimate. A recent study (Feng et al., 2018b) provided an extensive evaluation of the GlobCurrent dataset along the NWA continental shelves using long-term *in situ* current measurements over the MAB-GoM shelf region. The study showed that GlobCurrent products agree well with surface truth at both mean and seasonal scales on the broader shelf areas. However, agreement degrades nearing the coastlines and in the interior GoM. Potential issues affecting the quality of the GlobCurrent data inside the GoM were identified as inaccuracy in the MDT as well as ageostrophic factors, high altimeter measurement SSH noise, and overall gaps in satellite space and time sampling. Ultimately, GlobCurrent and conventional along-track altimeter data inaccuracies continue to limit their utility for investigation of 10-50 km scale topographically-steered and coastally-trapped currents that are central features within the Gulf of Maine and Scotian Shelf systems.

Fortunately, recent radar altimeter improvements offer hope for improved data. The new DDA/SAR altimeters offer lower SSH measurement noise and finer spatial resolution. Another development is a newly-improved global mean dynamic topography (MDT) product (Mulet et al., 2021) that synthesizes data from multi-mission altimeter products with up-dated geophysical corrections, orbit and geodesic geoid products, and a range of globally available ocean surface *in situ* current measurements. This MDT result gives more realistic mean currents near the coast and along the NW Atlantic shelf and its shelf break areas (Mulet et al., 2021). These improvements motivate this reexamination of satellite altimeter capabilities for resolving sea level variation associated with known 10-30 km scale coastal ocean circulation features in this shelf region.

3. Data and Methods

3.1. Altimetric and other datasets

- *Sentinel-3A altimeter data*

The Sentinel-3 (S-3) Synthetic Aperture Radar Altimeter (SRAL) operates at Ku- and C-band with the repeat cycle of 27 days with 385 orbits per cycle. Sea surface measurements by S-3 SRAL can be performed either in SAR mode or in LRM. SRAL altimeters on S-3A and S-3B, launched on 16 February 2016 and 25 April 2018, respectively, are now both operational. The S-3A orbit is similar to that of Envisat, allowing for continuation of the ERS/Envisat time series (https://sentinels.copernicus.eu/sentinel/missions/sentinel-3/satellite-description/orbit) (Fig. 1). S-3B operates in a new orbit with ground tracks that lie between two S-3A neighboring orbits to enhance spatial coverage. For this performance assessment, we focus on the S-3A data during a two-year period from 2018 to 2019, which is S-3A orbit cycles 26 to 52. Regional datasets using FFSAR altimeter data processing were generated at an 80-Hz posting rate (~80 m along-track resolution) using the retracking approach of Egido and Smith (2017) as applied to the S-3A SAR mode Level-1A data product that holds all the raw complex radar return echoes. Coincident S-3A SRAL Level 2 products of SAR and LRM (as needed reference) were obtained directly from the EUMETSAT data server. These L2 "standard" data files contain a set of geophysical parameters in the UFSAR mode and in the PLRM (pseudo-LRM) mode at both 20-Hz (~300 m) and 1-Hz (~7 km) posting rates.

(https://sentinels.copernicus.eu/web/sentinel/technical-guides/sentinel-3-altimetry/level-2-algorithms-products). In operation, the S-3 SAR mode observation is the default, and at the same time the estimated PLRM (equivalently called LRM) dataset are also available. This permits a desired comparison at the resolution and precision of the conventional pulse-limited radar altimetry for decades, served as a reference baseline for SAR mode assessments.

The key requisite range correction or adjustment parameters that include geophysical corrections, orbit altitude, and mean sea surface and that are used to estimate sea surface height (SSH) and its anomaly (SSHA) in this study are listed in Table 1. The same corrections are applied to FFSAR, UFSAR and PLRM data.

Upper-ocean current datasets used for assessment and validation include both gridded global data products and *in situ* measurements. These datasets are briefly described below.

- *Quasi-independent gridded ocean current products*

We use the absolute geostrophic vector currents from GlobCurrent (Rio et al., 2014) gridded at a resolution of ¼ degree in longitude by latitude (~25 km) at daily time step. These geostrophic velocities are computed from the absolute dynamic topography ADT=SSHA+ MDT, where the SSHA is from multi-altimeter-mission gridded analysis, and MDT is the latest released global product (Mulet et al., 2021), The GlobCurrent data products are described in http://marine.copernicus.eu/documents/QUID/CMEMS-MOB-QUID-015-003.pdf.

We also use ocean current data from a high-resolution Regional Ocean Modeling System (ROMS) analysis for the NSS-GOM-MAB shelves and adjacent Slope Sea region (Fig. 1b). The ROMS model is implemented with a 7-km horizontal resolution grid and 40-vertical layers, and uses 4-dimensional variational (4D-Var) data assimilation to incorporate observations from multiple altimeter SSHA datasets, including S-3A since April 2018, as well as numerous data from in situ coastal observations (Levin et al., 2018; Wilkin et al., 2018). Coregistration of S-3A ocean current estimates with these reference current datasets is described in Section 3.3.

- *Moored current observations in the GoM*

A set of current measurements at long-term moored buoys (I, E, B, M and N) in the GoM is available for S-3A assessment period (Fig. 1b) that acquire measurements hourly. Specific stations include buoys I, E, and B that are moored at the 60–70 m depth along the isobath that nominally aligns with the Maine Coastal current. Buoys M and N are moored in the deeper Jordan Basin and Northeast Channel locations, respectively. Each buoy measures currents through the water column using Acoustic Doppler Current Profilers (ADCP) as well as a near-surface doppler current sensor at 2 m. In this study, the *in situ* current measurements at the two buoys (I and M) situated within 15 km of S-3A satellite pass 747 (Figs. 1b and 8) are particularly useful for satellite data validation. Processing details of buoy current measurements are given in Section 3.3.

3.2. Performance metrics for SSH noise

Coincident S-3A datasets generated using the three different data processing approaches (LRM, UFSAR, FFSAR) are evaluated in the performance comparisons. We quantify their relative range measurement precision (i.e., noise level) by focusing on SSH and SSH-derived cross-track geostrophic current *Vg*. Metrics for SSH are described briefly here while those for SSH-derived *Vg* are given in Section 3.3.2.

First, the altimeter measurement noise level is estimated as the absolute value difference between consecutive along-track SSH values at a 20-Hz data rate as proposed by Cipollini et al. (2017). This is computed directly using the standard 20-Hz UFSAR and PLRM datasets. For the 80-Hz FFSAR data, we calculate a quasi-equivalent 20-Hz FFSAR SSH dataset by smoothing using a simple 1/20 second bin-averaging on the 80-Hz FFSAR SSH. In this way, the resultant 20-Hz FFSAR SSH shares the same data rate as UFSAR and PLRM, and can be used for further assessment.

Variations of the estimated noise for the three datasets are then evaluated in terms of distance to the coast in the region, particularly focusing on the shelf sea satellite passes where the water depth is less than 500m.

3.3. Estimated geostrophic current Vg and its assessment

3.3.1. Altimeter geostrophic current calculation

Based on the approach by Strub et al. (1997), the cross-track absolute geostrophic current *Vg* along each satellite ground track is estimated by the sea surface height gradients with a centered finite difference form of the geostrophic calculation,

$$Vg = \frac{g}{f}\frac{\partial(ADT)}{\partial(s)} = \frac{g}{f}\frac{ADT(j+N) - ADT(j-N)}{2N\Delta(s)} \quad (N > 0) \qquad (1)$$

where ADT is the Absolute Dynamic Topography used to calculate the absolute geostrophic current *Vg*, *f* is Coriolis parameter; *g* is the acceleration of gravity, *s* is along-track position, and *j* is the index of the along-track point. N is the half-span of the centered difference. For the 1-Hz data rate used in this analysis, Δs is roughly 7 km, the distance between two neighboring points along-track. Thus, N =1, 2, 3 represent the *Vg* along-track length scales of approximately 14 km, 28km and 42km, and the difference at each spatial span of 2N along-track intervals with 2N+1ground measurement points. The resultant velocities of *Vg* are then smoothed with an along-track running mean of 2N+1 values to reduce high frequency variability, forming the end product of cross-track geostrophic current *Vg* dataset.

There are two ways to calculate ADT used in Eq. (1): 1) ADT= SSHA +MDT, and 2) ADT= SSH–Geoid, where SSH is fully geo-physically corrected, that is SSH =Orbit_altitude–(Range +GeophysCorrs), and "Range" is only corrected for instrument effects. GeophysCorrs include all required geophysical corrections. SSHA (SSH Anomaly) =SSH-MSS (Mean Sea Surface) (the details of these parameters are given in Table 1). We have evaluated both of those. The simple evaluation tests (not shown) indicated that the errors of Geoid estimates are large near the coast particularly inside the GoM. In this study, we calculate *Vg* using ADT= SSHA+MDT unless stated.

Note that the simple centered finite difference used here is the direct and intuitive method to estimate cross-track geostrophic velocity *Vg* as shown in Eq.(1). Though this method is sub-optimal and more optimized difference operators exist (Powell and Leben 2004; Liu et al. 2012), this study attempts to evaluate the relative performance improvement on FFSAR and UNSAR over PLRM, as described below in Section 3.3.2.

For this purpose, it is sufficient to use the simple central difference of SSH for estimating *Vg*.

3.3.2. Altimeter Vg assessment

The following performance measures are used to assess Vg estimates.

- *Relative comparison between Vg products*

The standard deviation of *Vg*, *Vg_std*, is estimated for each individual processing approach (FFSAR, UFSAR, PLRM) with *Vg* estimates for N=1 (about 14-km along-track scale) at 1-Hz data rate. For an individual processing approach, *Vg_std* should represent the total variability of the estimated cross-track geostrophic current *Vg*, contributed mainly by *i*) the natural ocean current variability, and *ii*) by the expected error uncertainties of the *Vg* estimates including inherent range measurement noise, geophysical correction errors, and others. However, *Vg_std* difference between the *Vg* estimates by two different processing approaches is particularly useful for an objective precision comparison of the two different approaches.

Assuming the geophysical variability of current is not dependent on the processing approaches, the difference between *Vg_std* values can be considered an objective relative estimate precision between two different altimeter data products. Thus, the *Vg* noise reduction (in %) between two products A1 and A2 is defined by

$$Vg\ noise\ reduction_{A1vsA2} = \frac{(Vg_{\_std\_A1} - Vg_{\_std\_A2})}{(Vg_{\_std\_A1})} 100\% \qquad (2)$$

- *Comparison with quasi-independent reference current products*

As detailed above, two products *1)* GlobCurrent (GC) and *2*) the ocean currents from a regional ROMS circulation model are being used for altimeter S-3A *Vg* assessment. To co-locate the altimeter cross-track geostrophic current *Vg* with the two gridded reference current products, we extract the absolute geostrophic current components (*u*,*v*)=(eastward, northward) from daily GlobCurrent data, and depth-integrated upper surface 50-m mean current components (*u*,*v*) from the ROMS daily average output. These gridded current components are time/space interpolated onto the S-3A satellite track positions, and then projected onto the orientation normal to the S-3A track to generate relevant cross-track components. These are the daily V_{GC} for GlobCurrent, and two products, V_{ROMS_1davg} and V_{ROMS_3davg} for ROMS model. The latter V_{ROMS_3davg} is formed by applying a 3-day running average to the daily average fields (V_{ROMS_1davg}) to effectively remove tidal aliasing potentially present in the daily model fields.

For ROMS model output, the choice of the surface 50-m average currents and two time-average products is regarded to be reasonable when these are used to compare altimeter-derived surface geostrophic current products. We consider the choices is the best by now in terms of our previous studies (Feng et al., 2011, 2016) which found that the altimeter-based *Vg* showed the best agreement with the upper 50-m average current from Buoy M current measurements near the Northeast Channel.

- *Comparison with moored current observations in the GoM*

Buoy-altimeter current matchups at buoys M and I (Fig. 1b**)** are generated and used to assess altimeter-derived *Vg* accuracy. Matchup criteria are set so that the time difference between altimeter and buoy estimates is within one day and the spatial separation is within 15 km. To build the buoy-altimeter geostrophic current *Vg* matchup time series, the hourly buoy current components (u,v) time series are first processed to remove tidal current components predicted by the WebTide model (Dupont et al., 2005) with up to ten major tidal current components, and then projected onto the orientation normal to S-3A altimeter pass 747 to form the corresponding cross-track buoy current component. Next, one-day bin average processing is applied to hourly buoy current to form a daily time series of this component (V_{Buoy}). Finally, the resultant buoy V_{Buoy} time series is matched to the nearest day of S-3A satellite passage.

Two different buoy-measured current products are generated to compare with altimeter-derived absolute geostrophic current *Vg*. The first is the ADCP-measured current averaged over the water depths from 10-50m and 18-50m depth, $V_{Buoy(10\text{-}50m)}$ for buoy I and $V_{Buoy(18\text{-}50m)}$ for buoy M, respectively. The second is the near-surfaceV_{Buoy2m} obtained from Doppler current sensor measurements at 2 m for both buoys**.**

4. Results and Discussion

4.1. SSH noise for LRM, UFSAR and FFSAR data

Following Cipollini et al. (2017), the absolute difference of along-track consecutive SSH measurements at the effective 20-Hz posting rate (SSH=Orbit-Range, as provided in Table 1) is used as an objective indicator of the original instrument noise for SSH measurements. The assumption is that SSH is nearly invariant over a 300 m length scale, and thus this difference is primarily a measure of SSH (i.e. radar range) noise. Fig. 2a and 2b show SSH absolute noise estimates and relative SSH noise reduction improvement (in %) for the three SSH datasets. Estimates are derived in 1km binned segments versus the distance to the coast over all the S-3A altimeter passes (Fig. 1b) during the period of 2018-2019 where the water depth was 500m or less. The bin-median is used to minimize the impact of SSH outliers.

Results in Fig. 2a illustrate that *i*) noise in either SAR SSH dataset lies well below PLRM level (i.e., the conventional altimetry), *ii*) the FFSAR SSH noise level is about 1 cm below UFSAR, and *iii*) the FFSAR noise level remains at or below 3cm to within 1 km of the coast and only increases to ~4cm in the last 1-km bin. Comparing this to the UFSAR SSH noise estimates, one can see somewhat improved FFSAR performance from the coastline out to 5 km where both SAR altimeter datasets asymptote to their offshore (open ocean) noise levels.

The result that the observed S-3A UFSAR SSH noise change with distance to the coast is similar to recent CryoSat-2 UFSAR altimeter SSH noise analyses (Cipollini et al. 2017). Fig. 2b shows the relative noise reductions (in %) estimated using Eq. (2) for the cases, FFSAR vs. UFSAR, FFSAR vs. PLRM, and UFSAR vs. PLRM. When at least 5 km offshore, a 50%-70% SSH noise reduction is obtained using the UFSAR and FFSAR when compared to PLRM, respectively. Furthermore, FFSAR noise is approximately 25% below UFSAR. Another encouraging FFSAR result (Fig. 2b**)** is observed within ~5 km to the coast where the noise reduction improves greatly from 25% to 70% for FFSAR with respect to UFSAR.

The 25% improvement offshore between FFSAR and UFSAR agrees well with results recently reported in an open ocean study (Egido et al., 2021) where a 24% noise improvement was observed. However, the reason for the difference was not ascribed to focused vs. unfocused SAR reprocessing, instead, it was due to the chosen data posting rate difference where 20-Hz FFSAR data were found to be noisier than 80-Hz data (after the 80-Hz FFSAR data are smoothed and down-sampled to 20-Hz as we do in this paper). As discussed in Egido et al., (2021), the increased noise was due to inherent along-track radar return decorrelation differences.

Therefore, the findings here suggest that beyond 5 km from shore the FFSAR noise reduction is most likely contributed by the posting rate increase from 20-Hz to 80-Hz between the UFSAR and FFSAR data used in this study. But inshore of 5 km the FFSAR processing approach versus UFSAR shows further noise reduction near the coastlines that would not be explained by data posting rate. Within the 5-km coast with shorter-scale sea surface variability such as land and island-based disturbances the FFSAR processing is capable of generating less noise product. Certainly, both S-3A SAR SSH products are providing better performance than the conventional altimetry LRM in this NWA coastal shelf region. In the next section, we assess further potential benefits related to coastal shelf circulation applications.

4.2. Altimeter geostrophic current assessments

Performance measures defined in Section 3.3.2 are computed for each data product to compare altimeter-derived cross-track geostrophic currents (*Vg*) from the regional S-3A passes shown in Fig. 1b, using only data for depths less than 500m in order to focus on coastal shelf data quality. This focus essentially limits the data to measurements made north of the shelf break front that is highlighted in blue (Fig.1b).

4.2.1. Comparison between altimeter derived Vg estimates

Fig. 3 shows histograms of the cross-track absolute geostrophic current *Vg* derived from S-3A ADT, calculated using a 14-km along-track scale for the data aggregated over differing datasets. Three subregions to be considered are: the entire shelf region (ALL) ([36.0,48.0N], [75.0, 55.0W]), the Nova Scotian Shelf (NSS) ([42.0,45.0N], [66.0, 60.0W]) and Gulf of Maine (GoM) ([41.5, 44.5N], [70.0, 66.0W]). The mean (μ) and standard deviation (σ) of the aggregated *Vg* estimates for three altimeter datasets (in cm/s) are also shown.

For *Vg* derived from all three altimeter datasets, the mean μ of *Vg* is in the range from -3.2 to -2.7 cm/s for the case ALL (Fig. 3a). This negative velocity is consistent with the mean southwestward along-shelf current direction on the shelf, but the mean *Vg* magnitudes are somewhat lower than observations (Smith, 1983). This may be related to the fact that the cross-track geostrophic current *Vg* is nearly along shelf for ascending passes (from SE to NW) but not the descending (from NE to SW) (Fig. 1b). When only ascending track data are used for the analysis, *Vg* mean magnitudes slightly increase from -3.6 to -3.0 cm/s (not shown). The standard deviation σ of *Vg*, a measure of the total variability of *Vg* estimates, shows a consistent decrease when comparing the three datasets where PLRM > UFSAR > FFSAR in *Vg* σ across three subregions (Fig. 3a-c). Defined in Eq. (2), the relative *Vg* noise reduction (%) by one product A1 with respect to the another A2 is a relative objective precision measure between A1 and A2, and the results are given in Table 2. For the case ALL, the relative *Vg* noise reduction in UFSAR and FFSAR is 15.6%, and the relative noise reduction in PLRM with respect to either UFSAR or FFSAR product is much higher from 24% to 35.9%.

For a finer examination, statistics estimates are calculated for the cases of Nova Scotian Shelf and Gulf of Maine subregions, and presented in Fig. 3b and Fig. 3c, respectively. Results show that the mean μ and standard deviation σ in the NSS are quite similar to Fig. 3a. For the NSS, the SAR estimated means in the range from -3.3 to -3.9 cm/s (Fig. 3b) and from -3.8 to -4.5 cm/s if only ascending passes (from SE to NW) are considered (not shown). This range of NSS mean velocities generally agrees with the known observations (Smith, 1989; Loder et al., 2003; Hannah et al., 2001). In Fig. 3c, results differ somewhat for the case GoM in that the mean values are toward the small positives (0.6 to 0.8 cm/s) and the standard deviation values are significantly higher than those in NSS. The change in the mean velocity is not unexpected because inside the GoM there are many small–scale features (localized gyres and jets), and thus the across-track geostrophic currents are not always oriented southwestward. As noticed, the higher standard deviation σ of *Vg* in the GoM than in the NSS may reflect variability by the more diverse and shorter scale currents and not just from measurement noise. Regarding the relative noise reduction measure defined in Eq.2, the most apparent is the significant precision improvement in *Vg* from SAR (either FFSAR or UFSAR) dataset with respect to PLRM dataset for all three subregion cases (Table 2). For the inter-comparison of FFSAR and UFSAR, FFSAR does perform slightly better than UFSAR for all three sub-regions in the range from 5.7 % to 15.6% , and either SAR performs much better than LRM (Table 2).

4.2.2. Assessment of Vg against ocean current reference datasets

Here, the S-3A cross-track absolute geostrophic currents *Vg* from three products (FFSAR,UFSAR and PLRM) are estimated using 1-Hz data and a ~42 km length scale. The altimeter *Vg* products are compared to these reference currents V_{GC} for GlobCurrent ,and V_{ROMS_1davg} and V_{ROMS_3davg} for ROMS model.

Scatter plots of *Vg* against these current references are presented in Fig. 4, showing moderate correlations with R= 0.43-0.55 for *Vg* vs V_{GC} (Figs. 4a-c) and R =0.31-0.39 for *Vg* vs V_{ROMS_3davg} (Figs. 4d-f). Relatively small biases are in the range from -0.78 to -1.26 cm/s for V_{GC} (Figs. 4a-c) and from -0.63 to -1.17 cm/s for $V_{ROMS3davg}$ (Figs. 4d-f), respectively. In addition, the performance statistics of *Vg* vs. V_{ROMS_3davg} (Figs. 4d-f) is slightly better than that for *Vg* vs. V_{ROMS_1davg} (not shown). One can notice that the correlations between *Vg* and V_{GC} are greater than for *Vg* and V_{ROMS_3davg}, while the bias magnitudes are slightly larger for the former than for the latter. In short, the results are not surprising because both reference currents are not optimally used as ground truth for altimeter-based geostrophic current assessment.

In terms of this cross-comparison of the altimeter *Vg* products from the three differing processing datasets, it is clear that the highest correlation and the lowest bias are found for FFSAR-inferred *Vg* in each measure (Figs 4a and 4d). This assessment also indicates that the FFSAR does slightly outperform UFSAR in these performance statistics, while both improve significantly upon LRM data.

4.2.3. Validation with moored in-situ current measurements

The S-3A ascending pass 747 covers a very dynamic GoM area crossing Georges Bank and then Georges and Jordan basins before reaching the eastern Gulf coastline (Figs. 5 and 8**).** Two moored buoys (I and M) lie close to this pass, both within less than 15 km. Buoy M is moored at the center of Jordan's Basin while Buoy I is within the Maine Coastal current and near the eastern Maine coastline. Each buoy operates one down-looking ADCP to provide hourly measurements with 4-m to 8-m vertical resolution from the surface 10-m and 18-m down to the bottom for Buoy I and Buoy M, respectively, and another sensor provides near-surface (~2 m) current measurements, with nearly continuous measurements from 2018 to 2019.

Fig. 5a displays the time-latitude representation of the FFSAR based surface absolute geostrophic current (*Vg*) calculated along pass747 using a 28 km length scale and 1-Hz along-track data at the original 27-day (the S-3A repeat cycle) time sampling, without further temporal smoothing of the *Vg* estimates. Time covers a 2-year period (2018-2019) and space runs from the southern edges of the George's Bank to the eastern coast of the GoM (Figs. 5b and 8). Note that negative(in blue)/positive (in red) *Vg* values indicate the southwestward /northeastward current normal to the track throughout the Georges and the Jordan Basins (Fig. 5b). To our knowledge, this is the first single altimeter pass dataset to reveal such short spatial scale detail in cross-track altimeter-inferred absolute geostrophic currents inside the GoM.

While three-cycle data are missing over the 2-year period in this pass, the overall space and time information is revealing in several respects (Fig.5b). First, the narrow eastern MCC current is apparent at latitudes from 43.7N to the coast, and centers near 44.1N (also see Fig.8) . The magnitude and direction are consistent with this southwestward along-shelf current (negatives in blue). Next, a general counterclockwise gyre (of ~50 km length scale) spans Jordan Basin with its center near ~43.6N (also see Fig.8). Finally, the *Vg* data also indicate a clockwise gyre on Georges Bank (40.5 to 42N) and expected northeastward (positives in red) flow along Georges Basin (41.8N-42.6N). While these features persist, seasonal and spatial variations also appear in the altimeter SSH-resolved observations (Figs 5 and 8).

Figs. 6 and 7 show the instantaneous altimeter *Vg* vs. *in situ* V_{Buoy} (a) matchup time series, (b) and (c) the matchup scatter plots of S-3A *Vg* against $V_{Buoy(10\text{-}50m)}$ and V_{Buoy2m} for buoy I , and $V_{Buoy(18\text{-}50m)}$ and V_{Buoy2m} for buoy M, respectively. Three statistical measures (correlation R, bias B and RMSE) are used to quantify S-3A Vg performance, particularly identifying how performance differs among the three altimeter products.

By using buoy measurements as local ground truth for altimeter coastal ocean current assessment, we have tried to explore an optimal length scale used for S-3A *Vg* estimates. After experimenting with 14km, 28km, and 42km along-track scales, we found that the best spatial scale is 14km for the coastal buoy I and 28km for Jordan Basin buoy M in terms of the given performance measures. Not surprisingly, the findings imply that length scales used to infer cross-track geostrophic currents likely depend on the local length scale of currents. As described above the current length scale is relatively small at buoy I in the narrow eastern MCC while a length scale is a relatively large at buoy M site near the Jordan Basin gyre. Thus, optimal measurements maybe need to be utilized for determining an adaptive along-track length scale to derive *Vg* along a given pass rather than a constant scale. This topic is left for future studies.

For all three performance measures, the LRM-based *Vg* estimates are the worst amongst the three products without exception, while FFSAR performs slightly better than or similarly to UFSAR near both buoy sites. This result again indicates SAR-measured SSH can improve the derived geostrophic current significantly over the conventional LRM altimetry.

Noting specific details for buoy I comparison, it is found that the correlation is higher while the Bias and RMSE are greater for *Vg* vs. V_{Buoy2m} than for *Vg* vs. $V_{Buoy(10\text{-}50m)}$, respectively (Fig. 6c vs Fig. 6b). The performance of Vg_{FFSAR} is slightly better than Vg_{UFSAR}. Specifically, in Vg_{FFSAR} vs. $V_{Buoy(10\text{-}50m)}$ and in Vg_{FFSAR} vs. V_{Buoy2m}, R is 0.53 and 0.71, Bias is -0.026 and -0.044 m/s, and RMS is 0.098 and 0.082 m/s (Fig. 6b vs. Fig. 6c), respectively. The negatively-biased *Vg* indicates higher southwestward *Vg* than the buoy measurements. This is more apparent in year 2019 (Fig. 6a). The temporal varying patterns of altimeter *Vg* and $V_{Buoy(10\text{-}50m)}$ are visually correlated to some extent. Altimeter *Vg* agrees better with the surface buoy-measured V_{Buoy2m} in terms of correlation R and RMS at buoy I (Fig.6b).

Similar analysis at buoy M (Fig.7) finds that the altimeter SAR-based Vg_{FFSAR} and Vg_{UFSAR} time series show similar temporal patterns to the *in situ* buoy data, while the LRM *Vg* time series show larger and more frequent disagreement (Fig. 7a). Similar to the results at buoy I (Fig. 6), the performance of LRM *Vg* is apparently the worst in all three statistical measures at buoy M. Moreover, the SAR (FFSAR and UFSAR) *Vg* estimates show markedly better agreement with the depth-averaged current $V_{Buoy(18\text{-}50m)}$ (Fig. 7b) than for the surface 2m- measured V_{Buoy2m} (Fig. 7c) with no significant correlation. The statistical measures for Vg_{FFSAR} vs. $V_{Buoy(18\text{-}50m)}$ with R=0.61, Bias =-0.012 m/s and RMS =0.063 m/s look recognizably better than the ones for UFSAR *Vg* with R= 0.45, Bias =-0.014 m/s and RMS =0.055 m/s (Fig. 7b) at buoy M. The results suggest that the surface 2-m measured V_{Buoy2m} at buoy M (Fig.7c) likely contain a significant ageostrophic component such as that due to local wind forcing.

It is worth mentioning that these two independently measured currents, altimeter-derived geostrophic current *Vg* and buoy-measured current V_{Buoy}, are based upon totally different observational approaches. V_{Buoy} is directly measured current at one location, including geostrophic and potential ageostrophic contributions while altimeter *Vg* is inferred by altimeter–measured sea surface height gradient under the assumption of surface geostrophy. Thus, discrepancies in their direct comparison are not unexpected. Disagreement may stem from several altimeter error/uncertain sources, such as range noise, inaccuracy in geophysical corrections applied to altimeter sea surface height, mean sea surface and dynamic topography, and the along-track scale used for *Vg* estimates, as well as the altimeter-buoy co-location criteria (Feng et al., 2011, 2016).

Again, it is encouraging that this validation analysis in terms of *in-situ* current measurements confirms once more that DDA/SAR SSH-derived geostrophic currents provide a significant improvement over *Vg* derived from LRM SSH data (conventional altimetry). The validation analysis in this study provides the best agreement that has been ever shown to date between altimeter-based *Vg* and *in situ* measurements inside the GoM including its coastal zone, where the geostrophic currents are relatively weaker and more complex than for the MAB and Nova Scotian Shelf.

4.3. Demonstration of multiple single along-track analyses for Vg

To distinguish potential SAR skill compared to the conventional LRM data, the spatial content of altimeter *Vg* along a single given satellite pass is further examined. For this purpose, we selected several S-3A ascending passes in the shelf region because ascending passes are oriented nearly normal to the coastline and thus the cross-track current aligns with the along-shelf. Each selected pass crosses over well-documented small-scale current features like coastal currents, and shelf-sea gyres on the basins or banks. In this analysis, V_{GC} from GlobCurrent and V_{ROMS_3davg} the ROMS model 3-day running average velocity are also used for reference.

Fig. 8 displays the S-3A FFSAR-based current *Vg* mapping with four selected passes to represent a satellite overview of the across-track (approximately along-shelf) absolute geostrophic current on the shelf sea region in the early summer of 2018 (from May 24 to Jun 27, 2018). The altimeter-inferred *Vg* is estimated by using a 42-km length scale. This current field from S-3A FFSAR-inferred *Vg* clearly reveals a space-based snapshot, which is remarkably consistent with what has been reported in previous observations and modeling studies, including features such as NSS in-shore coastal current, eastern GoM coastal current, the deep shelf-break current from Nova Scotian Shelf to Georges Bank shelf breaks, as well as a set of small-scale gyres on the basins and banks in this shelf region (Townsend et al., 2006).

4.3.1. Pass 747 in the Gulf of Maine

Different from the time-latitude representation shown in Fig. 5, Fig. 8 displays an intuitive snapshot of the across-track geostrophic current field from FFSAR *Vg*, including pass 747 on 27 June 2018. The other S-3A *Vg* datasets along this track, as well as co-located reference current V_{GC} and V_{ROMS_3davg}, are shown in Fig. 9.

Several known small-scale current features are observed using the two SAR altimeter datasets along this pass (see Figs. 8 and 9). First, the southwestward along-shelf eastern Maine Coastal Current is well captured by both SAR-inferred *Vg* products near the coast (>43.7N) with a mean of ~12 cm/s and a max of ~19 cm/s. This estimate of the along-shelf summer period MCC velocity current is consistent with the in-situ current observational range of the sub-tidal surface current in the eastern MCC, from 15 to 30 cm/s (Pettigrew et al., 2005). Secondly, the data show a principally cyclonic circulation (i.e., Jordan Basin gyre) near the eastern GoM (43.0- 43.7N). Next, in Georges Basin, as expected a weak anti-clockwise gyre is present. Finally, on the south end of the pass, varying features over Georges Bank show that an expected nearly eastward flow on the northern flank of the Bank is captured (42.15N), aligning with the local isobath. The flow becomes southwestward on the Bank, gradually decreasing in magnitude with the near-zero current zone over the shallow mid- and southern Bank. The stronger southwest along-shelf flow is then observed near the shelf break (40.7N). To our knowledge, this is the first time that these Gulf of Maine circulation details have been so clearly revealed with single-pass satellite altimeter data.

The panels of Figs. 9b-d show velocities from all three S-3A *Vg* products. While similar, it is clear that the LRM-based *Vg* is much noisier along the track than for either SAR product, with distortions away from the SAR *Vg* in both spatial structure and magnitude. Fig. 9e shows the overlap of the FFSAR and PLRM *Vg* with GlobCurrent V_{GC} (green) and ROMS $V_{ROMS\text{-}3davg}$ (pink). Much stronger variation is observed in the altimeter-derived current than in either reference product, but their variations along the pass share some similarities. V_{GC} agrees slightly better with the SAR data than V_{ROMS_3davg} , and as another note, the along-track structures in V_{ROMS_3davg} agree better with the altimetry than V_{ROMS_1davg} (not shown). This suggests it is necessary to use a 3-day average on ROMS model daily data to remove tidal aliasing when comparing altimeter-based de-tided currents, at least for this GoM satellite pass.

The significant differences apparently observed between *Vg* and reference products of GlobCurrent and ROMS (Fig.9e) may be ascribed to several facts, including *i*) mismatch in the space and time resolutions among the *Vg* and the reference currents (GlobCurrent and ROMS), and *ii*) vertical and temporal averaging on ROMS outputs that do not well represent the surface geostrophic currents, (*iii)* interpolation errors near the coast, *(iv)* still existent issues on geophysical corrections applied to altimeter SSH, and so on. All these facts may impact the observed discrepancies collectively.

4.3.2. Pass 205 on the southwest Nova Scotian shelf off Cape Sable

S-3A ascending pass 205 crosses the shelf break near the Northeast Channel and traverses Browns Bank and the North Channel, before heading to the coast at Cape Sable. Nearest to the coast, the equatorward Nova Scotian Shelf Current typically takes a gradual turn into the GoM near Cape Sable. Fig. 8 also shows the current snapshot of the FFSAR-inferred *Vg*, measured on 8 June 2018 for the pass. Several prominent current signatures show up clearly along this section. Southwestward flow is observed on the coastal shelf off Cape Sable Shelf and over the North Channel (42.9N). There is also an obvious northeastward return flow on the northern part of Browns Bank in the zone (42.5N-42.8N). South of Browns Bank (42.5N), southwestward flow is seen that gradually increases toward the shelf break (42.0N).

As for pass 747 (Figs. 9b and 9c), the spatial variations in both SAR-inferred products are also remarkably similar for pass 205. For simplicity, the comparison focuses on the *Vg* FFSAR vs *Vg* PLRM plus the current references in Fig. 10b. In this case, the expanded along-track view more clearly illustrates the difference between the Vg_{PLRM} and Vg_{FFSAR} estimates. While each portrays similar flow reversals and their location in general, the PLRM-based Vg_{PLRM} is much noisier and apparently shows different along-track *Vg* structure, particularly nearest to the coast (>43.4N), but also approaching the shelf break (42.2N).

Regarding the comparison to reference currents (Fig. 10b), the spatial structure of FFSAR *Vg* does not agree with V_{GC}, but agrees fairly well with the ROMS V_{ROMS_3davg}. Significant disagreement of altimeter Vg with V_{GC} may be attributed to the coarse spatial resolution (~25km) in V_{GC} along the pass so that as low-resolution V_{GC} data cannot resolve the small-scale current features crossing such a dynamic shelf region.

How realistic is the summer period flow along this pass? First, the along-shelf coastal flow nearest Cape Sable is nominally associated with the fresh and cold water advection of the inner Nova Scotian Shelf Current that continues northwestward into interior GoM (Smith, 1983; Feng et al., 2016; Grodsky et al., 2020). Its variation depends on inflow magnitude and seasonality. The S-3A SAR-observed currents along the North Channel are similar with a mean magnitude nearing ~9cm/s. This inflow is only seen north of the North Channel, not unexpected in the summer because the SSC weakens and its transport into the GoM is reduced. The well-documented clockwise gyre on the Browns Bank is indeed revealed by the FFSAR-*Vg* data on this day. The Browns

Bank spatial structure captured by S-3A SAR mode measurements along this pass are generally consistent with previous observational and model studies (Smith, 1983; Smith et al.,1989; Hannah et al., 2001; Katavouta et al., 2016).

Based on satellite sea surface salinity observations, a recent study showed interannual modulation in this Nova Scotian shelf inflow to the GoM (Grodsky et al., 2021) where a significant fraction is attributed to anomalies in wind forcing. Use of these refined SAR altimeter measurements over the southwestern Nova Scotian Shelf may improve monitoring of this variability as it pertains to resulting freshwater impacts inside the Gulf of Maine.

4.3.3. Passes 547 and 005 on the Nova Scotian Shelf

Two S-3A passes crossing the NSS are selected for assessment. The mean circulation on this shelf varies at several spatial scales. The overall flow is characterized by a southwestward along-shelf current with the two key branches. The in-shore SSC current discussed earlier originates in the Gulf of St. Lawrence and continues southwestward along the Scotian coastline (as described for pass 205, Figs. 8 and 10). The offshore branch originates as a down-stream extension of the Labrador Current, and continues along the Scotian shelf and its shelf break front region. Knowledge of variations in these flows is critical to understanding the down-stream circulation in the GoM-MAB shelf system. Thus, both modelers and coastal oceanographers have a strong interest in Scotian Shelf observational datasets including highest accuracy satellite altimeter sea surface measurements.

The regional map with FFSAR-*Vg* along passes 547 (24-May-2018) and 005 (1-Jun-2018) is also shown in Fig. 8. The other S-3A Vg data and reference currents are displayed in Figs. 11 and 12, respectively. The FFSAR-inferred *Vg* shows the cross-track absolute geostrophic current *Vg* is aligned well with orientation of the coast and shelf break. Keep in mind that the inter-track distance between the two passes is about 150 km and that the time difference between the measurements from the two passes is seven days. The spatial structure of the along-shelf current revealed by FFSAR *Vg* along both passes appears highly coherent across the shelf (Fig. 8). As with earlier analyses, there are significant LRM-based *Vg* differences from the SAR-based data both near the coastline and near the shelf break. There looks obvious noise increase in Vg_{PLRM} (Figs. 11b and 12b), particularly along pass 005 where the sign of the Vg_{PLRM} current opposes the SAR Vg_{FFSAR} near the coastline (Fig. 12b).

The key circulation features observed with S-3A SAR observations can be detailed by Fig. 8 and referencing Figs. 11 and 12 for passes 547 and 005, respectively. First, the inshore SSC branch shows a consistent SW flow aligned shoreward of the 150 m isobath (> 44.1N) between the western edge of Emerald Basin and LaHave Basin along pass 547 (Fig. 11) and inside the 150m isobath (>44.4N) on the north rim of the Middle Bank along pass 005 (Fig. 12). Secondly, much stronger southwestward flow is observed over the off-shore shelf break and slope sea where there is high *Vg* coherence between the two passes (Figs. 8,11, and 12).

Interestingly, between the inshore and offshore shelf break SW flows, there exists an obvious northeastward return flow detected with both the SAR and PLRM based *Vg* data along both passes. Focusing on pass 547 (Figs. 8 and 11), the return flow is relatively weaker in a mean magnitude (3-4cm/s) and occurs near the southern flank of

Emerald Basin (~43.5N). At the latitude zone (43.7N-44.05N) there is nearly no across-track current (<1cm/s in mean). This area is a deep channel in the nearly north-to-south direction between Lahave and Emerald Basins. As shown by a modeling result (Hannah et al., 2001), a cross shore branching in the current break from the in-shore NSS Current to move roughly southward offshore over the western edge of Emerald Basin with little across-track (NE-to-SW) current component. But a small-scale gyre exists around the Emerald Basin, the returning flow seen at the southern flank zone on the Emerald Basin can be considered part of the gyre.

It is worth noting that S-3A pass 547 is fairly close to a well sampled cross-shelf oceanographic transect called "the Halifax section", where long-term hydrographic observations are collected (Loder et al., 2003; Dever et al., 2016). Their data confirm the plausibility of these late May NSS Current and the return flow *Vg* estimates derived from the S-3A data. Loder et al. (2003) found similar the seasonal variation in the alongshelf density-driven geostrophic current on the Halifax section. Specifically, a significant and nearly continuous inner-shelf surface-intensified southwestward flow, strongest in winter (peak near 30 cm/s) and the weakest in summer (peak of 10–15 cm/s). The mean current magnitude (~10cm/s) observed by the S-3A SAR is generally consistent with these observations and numerical modeling results (Hannah et al., 2001; Katavouta et al., 2016).

Secondly, a weak predominantly northeastward (return) flow appears over Emerald Bank. This return flow is likely consistent with the shelf-edge flow making an onshore meander that moves counterclockwise around Emerald Basin (Thompson and Griffin, 1998; Hannah et al., 2001; Loder et al., 2003). In comparison with reference currents (Figs. 11b-12b), SAR-based Vg_{FFSAR} agrees in some degree with V_{GC} in pass 547 (Fig. 11b) and fairly well with V_{GC} in pass 005 (Fig. 12b) on the shelf likely because longer coherent length scales on this shelf are well suited for their merged-altimeter SSH interpolation scheme of GlobCurrent products. However, V_{GC} on both passes appear no data close to the coast most likely due to its coarse spatial resolution (~25 km). One can see that the SAR-based *Vg* agrees poorly with ROMS model V_{ROMS_3davg} (Fig. 11b). This discrepancy may occur because this pass is located near one boundary of this ROMS model domain (Fig. 1).

Upstream 150km from pass 547, the altimeter data on pass 005 (Figs. 8 and 12) show the return current is stronger than on pass 547 and appears over the Western Bank to Middle Bank area (43.8-44.4N), with the mean magnitude of ~7.5cm/s. This feature reflects a general clockwise circulation comprising the shelf-edge throughflow and a partial gyre on Western Bank that is generally consistent well with modeling results (Hannah et al., 2001).

5. Summary

In this paper, we have reviewed recent satellite altimeter data application and assessment studies for the Nova Scotian Shelf, the Gulf of Maine, and the Mid Atlantic Bight system, and then focused on evaluation of newly available Delay Doppler SAR altimetry data from the Sentinel-3A satellite. This study quantifies that SAR processing of the S-3A data measurably improves altimeter-measured SSH and SSH-derived geostrophic velocity estimates in comparison to the conventional Low Resolution Mode (LRM). It also illustrates where FFSAR-processed data can potentially outperform the present standard UFSAR data. Most importantly, we have concluded that the new S-3 DDA/SAR mode data can provide improved accuracy in resolving narrow along-shelf currents and other small scale features (scales less than 40 km) that have been difficult to discern using conventional LRM data.

Measurable improvements are observed in several respects using SAR mode altimetry across this Northwestern Atlantic shelf ocean region. First, SAR mode SSH measurements provide much lower noise (reduced by 55-70%) compared to the S-3A LRM measurements. Secondly, the FFSAR SSH noise level is about 1cm lower than UFSAR (reduced by ~25%) when offshore by more than 5km. This observed 25% improvement is consistent with the results recently reported by Egido et al. (2021) who showed that this level of SSH precision improvement can be attributed to the native data posting rate difference (80 Hz being more optimal than 20 Hz) rather than to FFSAR vs. UFSAR data processing retracking approaches. But an apparent benefit from the fully-focused SAR processing is observed within 5 km of the coast where one expects shorter-scale ocean surface variability, land and island-based disturbances appear to generate less noise in the FFSAR product. Within 5 km of the coast, the FFSAR versus UFSAR noise reduction is significant, with observed levels between 25%-70%. Third, the absolute geostrophic current estimates derived using FFSAR show the lowest noise level in all evaluations - versus *in situ* and reference current datasets, and in qualitative along-track comparisons. In fact, FFSAR data slightly outperform the UFSAR in all test assessments performed in this study. The largest advantage revealed in the present analyses comes when using either SAR mode dataset in comparison to the conventional LRM data, an expected but nevertheless encouraging result.

Finally, multiple single satellite S-3A track examples are selected to illustrate the most apparent advantage that the lower noise SAR-based SSH data can provide on high quality of altimeter-inferred geostrophic current products. Namely, the realistic fine-scale spatial structure and amplitudes of SAR altimeter-derived geostrophic currents indicate the capability to more clearly reveal 20-40 km scale coastal currents and topographically-steered gyres on the Nova Scotian Shelf and inside the Gulf of Maine. In particular, the DDA/SAR data reveal signals pertaining to two regionally-important currents, the Maine Coastal and Nova Scotian Shelf currents that are resolved using S-3A SSH-based current estimates derived using either the FFSAR or UFSAR product. This opens new regional monitoring possibilities using the combination of presently orbiting SAR altimeters that includes Sentinel-3A, Sentinel-3B and Sentinel-6 Michael Freilich.

Acknowledgements

This research was supported by NOAA via the NASA-NOAA Joint program announced in NASA Research Announcement (NRA) NNH16ZDA001N, Research Opportunities in Space and Earth Science (ROSES-2016), Program Element A.11: Ocean Surface Topography Science Team (OSTST) and by NASA OSTST grant NNX17AH58G. This research has been supported by NOAA grant NA16NOS0120020. We thank the NOAA Integrated Ocean Observing System (IOOS) program office and the Northeast Regional Association of Coastal Ocean Observing Systems (NERACOOS) for providing the buoy observations.

References

Brickman, D., Wang Z., DeTracey, B., 2016. Variability of current streams in Atlantic Canadian Waters: A model study. Atmosphere-Ocean 54, 218-229. https://doi.org/10.1080/07055900.2015.1094026.

Brown W. S., Irish, J. D., 1993. The annual variation of water mass structure in the Gulf of Maine: 1986–87. J. Mar. Res. 51, 53–10. https://doi.org/10.1357/0022240933223828.

Cipollini, P., Calafat, F. M., Jevrejeva, S., Melet, A., Prandi, P., 2017. Monitoring Sea Level in the Coastal Zone with Satellite Altimetry and Tide Gauges. Surv Geophys. 38, 33–57. https://doi.org/10.1007/s10712-016-9392-0.

Csanady, G. 1978. The arrested topographic wave. J. Phys. Oceanogr. 8, 47–62. https://doi.org/10.1175/1520-0485(1978)008<0047:TATW>2.0.CO;2

Dever, M., Hebert,D., Greenan, B.J., Sheng., J., Smith, P.C., 2016. Hydrography and Coastal Circulation along the Halifax Line and the Connections with the Gulf of St. Lawrence, Atmosphere-Ocean 54, 199-217. https://doi.org/10.1080/07055900.2016.1189397

Dinardo, S., Fenoglio-Marc, L., Buchhaupt, C., Becker, M., Scharroo, R., Fernandes, M.J., Benveniste, J., 2018. Coastal SAR and PLRM altimetry in German Bight and West Balt. Adv. Space Res. 62, 1371-1404. https://doi.org/10.1016/j.asr.2017.12.018.

Dupont, F., Charles, G. Hannah, G. Greenberg, D., 2005. Modeling the sea level of the upper Bay of Fundy. Atmosphere-Ocean 43, 33–47. https://doi.org/10.3137/ao.430103.

Egido, A., Smith, W. 2017. Fully Focused SAR Altimetry: Theory and Applications. IEEE Trans. Geosci. Remote. Sens. 55, 392–406. https://doi.org/10.1109/TGRS.2016.2607122.

Egido, A. Dinardo, S., and Ray, C., 2021. The case for increasing the posting rate in delay/Doppler altimeters, Adv. Space Res. 68, 930–936. https://doi.org/10.1016/j.asr.2020.03.014.

Feng, H., Egido, A., Vandemark, D., Dufau, C., 2018a. Can fully-focused or unfocused SAR delay Doppler altimeter range data provide enhanced detection of coastal currents in the Nova Scotia Shelf?. OSTST meeting, Azores Archipelago, Portugal, Sept 2018. Available online https://ostst.aviso.altimetry.fr/fileadmin/user_upload/tx_ausyclsseminar/files/Feng_etal_PosterFFSAR_OSTST2018_final.pdf.

Feng, H., Vandemark, D., 2011. Altimeter data evaluation in the coastal Gulf of Maine and Mid-Atlantic Bight Regions. Mar. Geodesy. 34, 340–363. https://doi.org/10.1080/01490419.2011.584828.

Feng, H., Vandemark, D., Wilkin, J., 2016. Gulf of Maine salinity variation and its correlation with upstream Scotian Shelf currents at seasonal and interannual time scales. J. Geophys. Res. Oceans. 121, 8585–8607. https://doi.org/10.1002/2016JC012337.

Feng, H., Vandemark, D., Levin, J., Wilkin, J., 2018b. Examining the Accuracy of GlobCurrent Upper Ocean Velocity Data Products on the Northwestern Atlantic Shelf. Remote Sens.10, 1205. https://doi.org/10.3390/rs10081205.

Fenoglio-Marc, L., Dinardo, S., Scharroo, R., Roland, A., Sikiric, M.D., Lucas, B., Becker, M., Benveniste, J., Weiss, R., 2015. The German Bight: A validation of CryoSat-2 altimeter data in SAR mode. Adv. Space Res. 55, 2641-2656. https://doi.org/10.1016/j.asr.2015.02.014.

Fu, L.L., Cazenave, A., 2001. Satellite altimetry and earth sciences: A handbook of techniques and applications. Academic Press, San Diego. https://www.elsevier.com/books/satellite-altimetry-and-earth-sciences/fu/978-0-12-269545-2.

Geyer, W. R., Signell, R. P., Fong, D. A., Anderson, D. M., Keafer, B. A., 2004. The freshwater transport and dynamics of the Western Maine Coastal Current. Cont. Shelf Res. 24, 1339–1357. https://doi.org/10.1016/j.csr.2004.04.001.

Grodsky, S. Vandemark, D., Feng, H., Levin, J., 2018. Satellite detection of an unusual intrusion of salty slope water into a marginal sea: using SMAP to monitor Gulf of Maine inflows. Remote Sens. Environ. 217,550-561. https://doi.org/10.1016/j.rse.2018.09.004.

Grodsky, S. Vandemark, D, Feng, H., 2018. Assessing coastal SMAP surface salinity accuracy and its application to monitoring Gulf of Maine circulation dynamics. Remote Sens.10, 1232. https://doi.org/10.3390/rs10081232.

Grodsky, S., Vandemark, D., Reul, N., Feng, H., and Levin, J., 2021. Winter surface salinity in the northeastern Gulf of Maine from five years of SMAP satellite data. J. Mar. Sys. 216, 103508. https://doi.org/10.1016/j.jmarsys.2021.103508.

Guccione, P., Scagliola, M., and Giudici, D., 2018. 2D Frequency Domain Fully Focused SAR Processing for High PRF Radar Altimeters. Remote Sens. 10(2), 1943. https://doi.org/10.3390/rs10121943.

Han, G., 2007. Satellite observations of seasonal and interannual changes of sea level and currents over the Scotian Slope. J. Phys. Oceanogr. 37, 1051–1065. https://doi.org/10.1175/JPO3036.1.

Han, G., Tang, C. L., Smith, P. C., 2002. Annual Variations of Sea Surface Elevation and Currents over the Scotian Shelf and Slope. J. Phys. Oceanogr. 32(6), 1794-1810. https://doi.org/10.1175/1520-0485(2002)032<1794:AVOSSE>2.0.CO;2

Hannah, C., G., Shore, J., Loder, J. W., Naimie, C. E., 2001. Seasonal circulation on the western and central Scotian Shelf. J. Phys. Oceanogr. 31, 591–615. https://doi.org/10.1175/1520-0485(2001)031<0591:SCOTWA>2.0.CO;2.

Katavouta, A., Thompson, K.R., Lu, Y., Loder, J., 2016. Interaction between the Tidal and Seasonal Variability of the Gulf of Maine and Scotian Shelf Region. J. Phys. Oceanogr. 46, 3279-3298. https://doi.org/10.1175/JPO-D-15-0091.1

Lentz, S., 2008. Observations and a model of the mean circulation of the Mid-Atlantic Bight continental shelf. J. Phys. Oceanogr. 38, 1203-1221. https://doi.org/10.1175/2007JPO3768.1.

Levin, J., Wilkin, J., Fleming, N., Zavala-Garay, J., 2018. Mean circulation of the Mid-Atlantic Bight from a climatological data assimilative model. Ocean Model. 128, 1–14. https://doi.org/10.1016/j.ocemod.2018.05.003.

Levin, J., Arango, H. G., Laughlin,B., Wilkin, J., Moore, A. M., 2021. The Impact of Remote Sensing Observations on Cross-Shelf Transport Estimates from 4D-Var Analyses of the Mid-Atlantic Bight. Adv. Space Res. 68, 553-570. https://doi.org/10.1016/j.asr.2019.09.012.

Liu, Y., Weisberg, R.H., Vignudelli, S., Roblou, L., Merz, C.R., 2012. Comparison of the X-TRACK altimetry estimated currents with moored ADCP and HF radar observations on the West Florida Shelf. Adv. Space Res. 50, 1085-1098. https://doi.org/10.1016/j.asr.2011.09.012.

Liu, Y., Weisberg, R.H., Vignudelli, S., Mitchum, G.T. 2014. Evaluation of altimetry-derived surface current products using Lagrangian drifter trajectories in the eastern Gulf of Mexico. J. Geophys. Res. Oceans, 119, 2827-2842. https://doi.org/10.1002/2013JC009710.

Loder, J.W., Hannah, C.G., Petrie, B. D., Gonzalez, E. A., 2003. Hydrographic and transport variability on the Halifax section. J. Geophys. Res. Oceans. 108, 8003. https://doi.org/10.1029/2001JC001267.

Pettigrew, N. R., Churchill, J. H., Janzen, C. D., Mangum, L. J., Signell, R. P., Thomas, A. C., Townsend, D. W., Wallinga, J. P., Xue, H., 2005. The kinematic and hydrographic structure of the Gulf of Maine Coastal Current. Deep Sea Res., Part II, 52, 2369–2391. https://doi.org/10.1016/j.dsr2.2005.06.033.

Martin-Puig C., Ruffini, G., 2009. SAR altimeter retracker performance bound over water surfaces. IEEE International Geoscience Remote Sensing Symposium, 2009, 449-452. Available online https://doi.org/10.1109/IGARSS.2009.5417633.

Mulet, S., Rio, M.-H., Etienne, H., Artana, C., Cancet, M., Dibarboure, G., Feng, H., Husson, R., Picot, N., Provost, C., Strub, P. T., 2021. The new CNES-CLS18 Global Mean Dynamic Topography. Ocean Sci. 17 ,789-808. https://doi.org/10.5194/os-17-789-2021.

Powell, B.S., and Leben, R.R., 2004. An optimal filter for geostrophic mesoscale currents from along-track satellite altimetry. J. Atmos. Oceanic Technol. 21, 1633-1642. https://doi.org/10.1175/1520-0426(2004)021<1633:AOFFGM>2.0.CO;2

Raney, R. K., 1998. The delay/Doppler radar altimeter. IEEE Trans. Geosci. Remote Sens. 36,1578-1588. https://doi.org/10.1109/36.718861.

Raney, R. K., 2012. CryoSat SAR-mode looks revisited. IEEE Geosci. Remote Sens. Lett. 9, 393–397. https://doi.org/10.1109/LGRS.2011.2170052.

Ray, C., Martin-Puig, C., Clarizia, M.P., Ruffini, G., Dinardo,S., Gommenginger, C., Benveniste, J., 2015. SAR Altimeter Backscattered Waveform Model. IEEE Trans. Geosci. Remote Sens. 53(2). https://doi.org/10.1109/TGRS.2014.2330423.

Rio, M.-H., Mulet, S., Picot, N., 2014. Beyond GOCE for the ocean circulation estimate: Synergetic use of altimetry, gravimetry, and in situ data provides new insight into geostrophic and Ekman currents. Geophys. Res. Lett. 41, 8918-8925. https://doi.org/10.1002/2014GL061773.

Shan, S., Sheng, J., Ohashi, K., Dever, M., 2016. Assessing the performance of a multi-nested ocean circulation model using satellite remote sensing and in situ observations. Satellite Oceanogr. Meteor. 1, 39–59. http://dx.doi.org/10.18063/SOM.2016.01.004.

Smith, P. C., 1983.The mean and seasonal circulation off southwest Nova Scotia. J. Phys. Oceanogr. 13, 1034–1054. https://doi.org/10.1175/1520-0485(1983) 013<1034: TMASCO>2.0.CO;2.

Smith, P. C., 1989. Circulation and dispersion on Browns Bank. Can. J. Fish. Aquat. Sci. 46:4, 539–559. https://doi.org/10.1139/f89-073.

Smith P. C., Houghton, R. W., Fairbanks, R. G., Mountain, D. G., 2001. Interannual variability of boundary fluxes and water mass properties in the Gulf of Maine and on Georges Bank: 1993-1997. Deep Sea Res, Part II: Topical Studies in Oceanography 48, 37–70. https://doi.org/10.1016/S0967-0645(00)00081-3.

Thompson, K. R., Griffin, D. A., 1998. A model of the circulation on the outer Scotian Shelf with open boundary conditions inferred by data assimilation. J. Geophys. Res. Oceans.103,C13, 30,641– 30,660. https://doi.org/10.1029/98JC01765.

Townsend, D.W., Thomas, A.C., Mayer, L.M., Thomas, M.A., Quinlan, J.A, 2006. Oceanography of the Northwest Atlantic Continental Shelf. In The Sea; Robinson, A.R., Brink, K.H., Eds.,119–168. Harvard University Press: Cambridge, MA, USA.

Townsend, D. W., Pettigrew, N. R., Thomas, M. A., Neary, M. G., McGillicuddy, D. J., O'Donnell, J., 2015. Water masses and nutrient sources to the Gulf of Maine, J. Mar. Res.73, 93–122. https://doi.org/10.1357/002224015815848811.

Urrego-Blanco, J., Sheng, J., 2014. Study on subtidal circulation and variability in the Gulf of St. Lawrence, Scotian Shelf, and Gulf of Maine using a nested-grid shelf circulation model, Ocean Dyn. 64(3) 385–412. https://doi.org/10.1007/s10236-013-0688-z.

Vignudelli, S., Kostianoy, A., Cipollini, P., Benveniste, J. (Eds.), 2011. Coastal altimetry (1st ed.). Springer Berlin Heidelberg, Berlin, Heidelberg. https://doi.org/10.1007/978-3-642-12796-0.

Wilkin, J., Levin, J., Lopez, A., Hunter, E., Zavala-Garay, J., Arango, H., 2018. A Coastal Ocean Forecast System for the U.S. Mid-Atlantic Bight and Gulf of Maine. In New Frontiers in Operational Oceanography, Chassignet E., Pascual, A., Tintoré, J., Verron, J. (Eds.), GODAE OceanView, 593-624. https://doi.org/10.17125/gov2018.ch21.

Table 1

Summary of Sentinel-3A SRAL altimeter datasets used in this study (cycles 26-52 spanning years 2018-2019)

<table>
<tr><td>FFSAR (this study)
(80 Hz; ~70 m)
Fully-Focused SAR (FFSAR)</td><td>SRAL L2 (EUMESAT)
(1 Hz, ~7 km; 20 Hz, ~300 m)
Un-Focused SAR (UFSAR)
Pseudo-LRM (PLRM)</td></tr>
<tr><td colspan="2">Range, SSH[a], SSHA[b],Geoid, Orbit_altitude, GeophyCorrs[c], MSS[d]</td></tr>
<tr><td>Goodness of fit</td><td>Quality flags of parameters
rms in range, SSH,</td></tr>
<tr><td colspan="2">• Range: instrument correction applied.
• Orbit_altitude; in GDR-F standard
• SSH[a] (Sea surface Height) =Orbit_altitude –Range
• SSHA[b] (Sea surface Height Anomaly)=SSH-(Range +GeosCorrs)-MSS
• GeophyCorrs[c] = (dry_tropo_ecmwf+wet_tropo_rad+iono_alt_smooth+inv_bar_mog2d+ tide_solid+tide_ocean_fes14 +tide_load_fes14 + ssb_cls)
• MSS[d] (Mean Sea Surface)=MSS_DTU18 (Mulet et al., 2021)
• rms[e] (of parameters is in 1Hz, estimated with valid data at 20Hz data posting rate</td></tr>
</table>

Table 2

Overall relative noise reduction in *Vg* estimates (in %), defined in Eq. (2), by one altimeter dataset A1 with respect to the another A2 from three altimeter products (FFRAR UFSAR, PLRM) for the three subregions: ALL (the entire shelf region), NSS (Nova Scotian Shelf) and GoM (Gulf of Maine) (see details in Section 4.2.1.)

A1 vs A2	Regional datasets		
	ALL	NSS	GoM
UFSAR vs. FFSAR	15.6	5.7	12.1
PLRM vs. FFSAR	35.9	34.8	37.9
PLRM vs. UFSAR	24.0	30.1	29.3

Fig1a. Map of the study region on the northwest Atlantic shelf with the contours of 100, 200, 1000 and 4000 m isobaths. Thick blue arrows show a schematic representation of the circulation in this shelf region. Abbreviations are used to denote Jordan Basin (JB), Wilkinson Basin (WB), Georges Basin (GB), Northeast Channel (NEC), Northern Channel (NC), Great South Channel (GSC), and Mid Atlantic Bight (MAB).

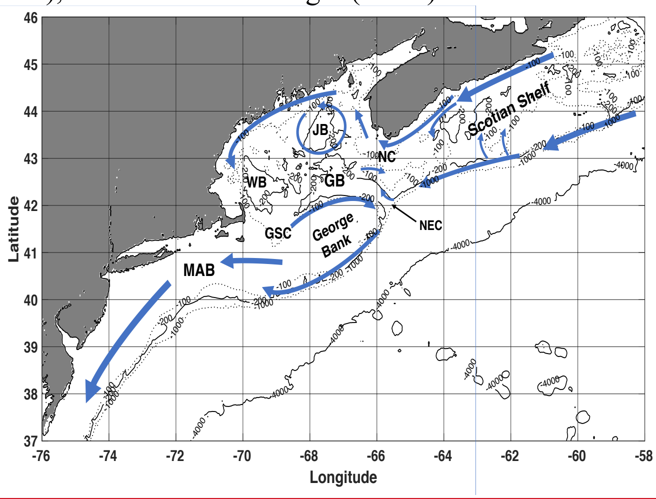

Fig.1b. Map of the study region with bathymetric contours. Solid lines represent Sentinel-3A (S-3A) SRAL altimeter ground tracks one of which T747 is labeled. Also shown are the positions of six NERACOOS buoys (red solids) labeled with letters (N, L, M, I, E, and B). Gray stippled area is the domain of ROMS regional circulation model. Abbreviations used here are the same as in Fig1a.

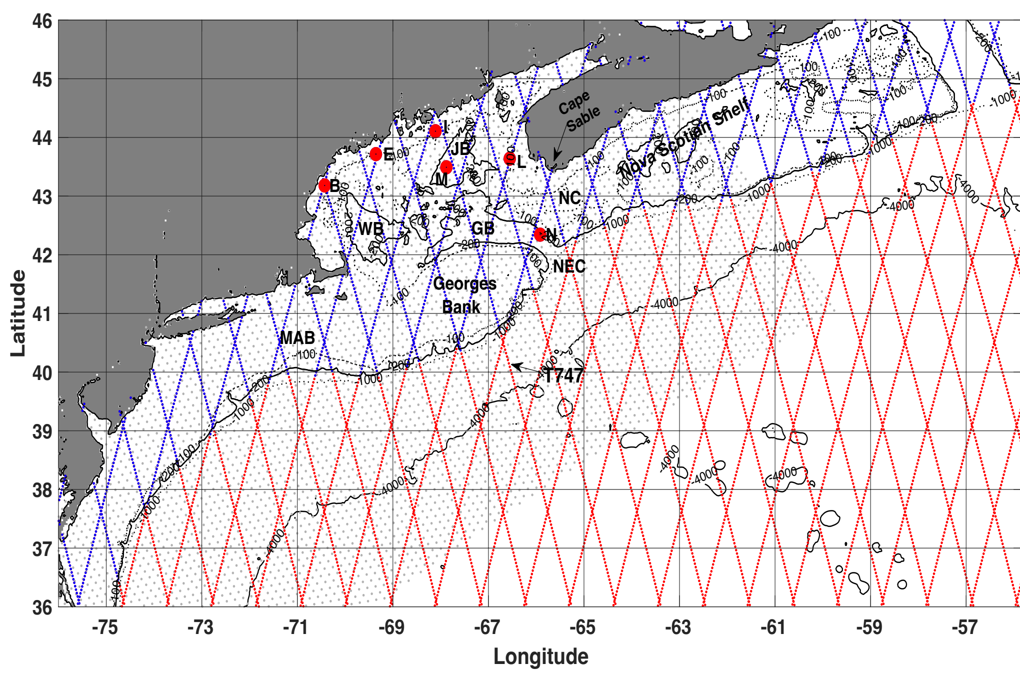

Fig. 2. (a) Along-track rms SSH noise (cm) and (b) relative rms noise reduction (%) within 1-km bins versus distance to the coast. Noise is estimated as the absolute difference between consecutive 20-Hz measurements as defined in Section 3.2. Results are shown for three datasets using the FFSAR, UFSAR and LRM processing approaches. The SSH data are screened using a retracking goodness of fit threshold <=0.05 for FFSAR and QC SSH quality=0 for UFSAR and PLRM.

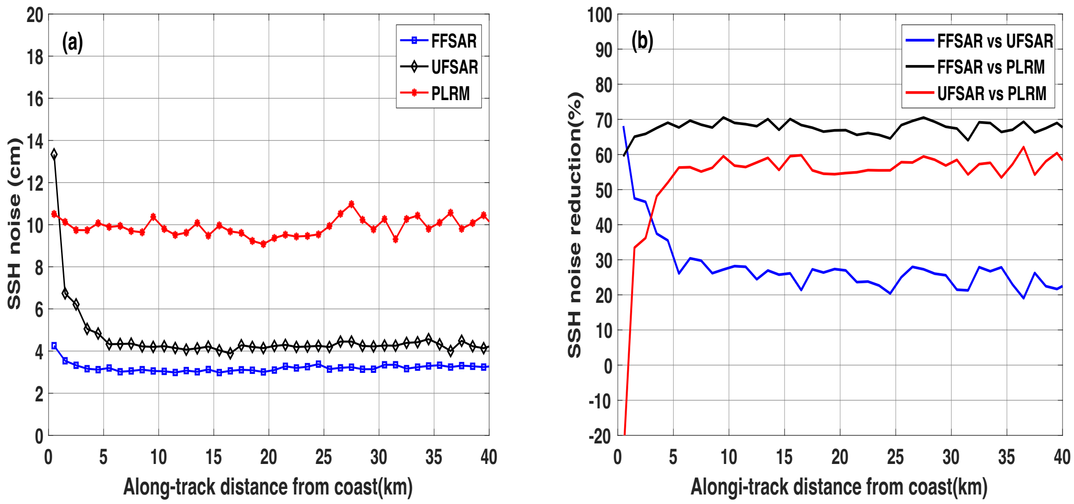

Fig. 3. Histograms of the cross-track absolute geostrophic current *Vg* derived from the absolute dynamic topography ADT=SSHA+MDT by using 1-Hz data from altimeter products (FFSAR, UFSAR, and PLRM). *Vg* is calculated using a 14 km length scale in Eq. (1) (see details in Section 3.3.1.). Panels (a) (b) (c) represent the results from the reginal datasets of All (all region), NSS(Nova Scotian Shelf), and GoM (Gulf of Maine), respectively. Note that *Vg* mean (μ) and standard deviation (σ) values (in cm/s) are given in each legend.

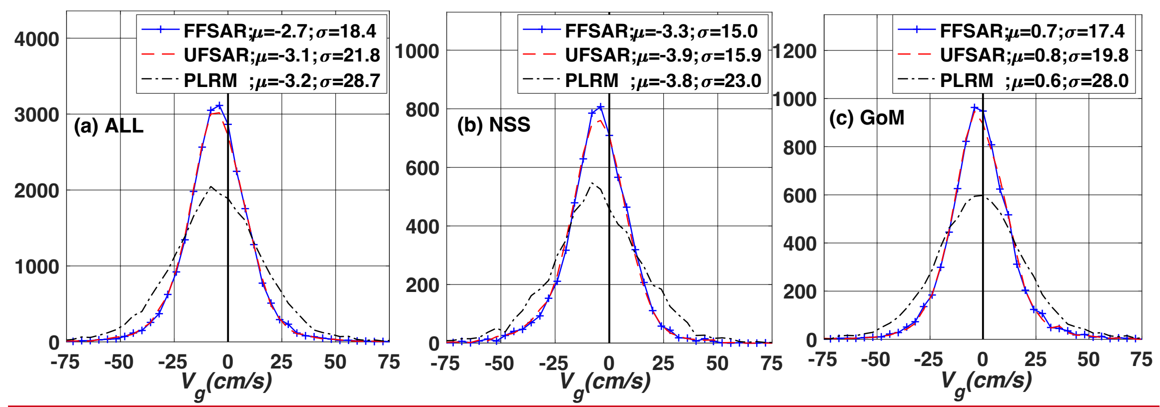

Fig. 4. Contoured scatter plots of S-3A cross-track absolute geostrophic current *Vg* estimated by using a 42 km length scale in terms of 1-Hz data from altimeter products, (a) and (d) for FFSAR, (b) and (e) for NFSAR, and (c) and (f) for PLRM against the reference current products GlobCurrent absolute geostrophic cross-track V_{GC} (the 1st. row) and the 50m depth-averaged and 3-day averaging V_{ROMS_3davg} from ROMS regional circulation model (the 2nd row) . The correlation coefficient (R) and bias (B) in cm/s are also provided in the legends. Contours represent normalized 2D data population distributions. Note that all correlation coefficients reported here are statistically significant with p values close to zero.

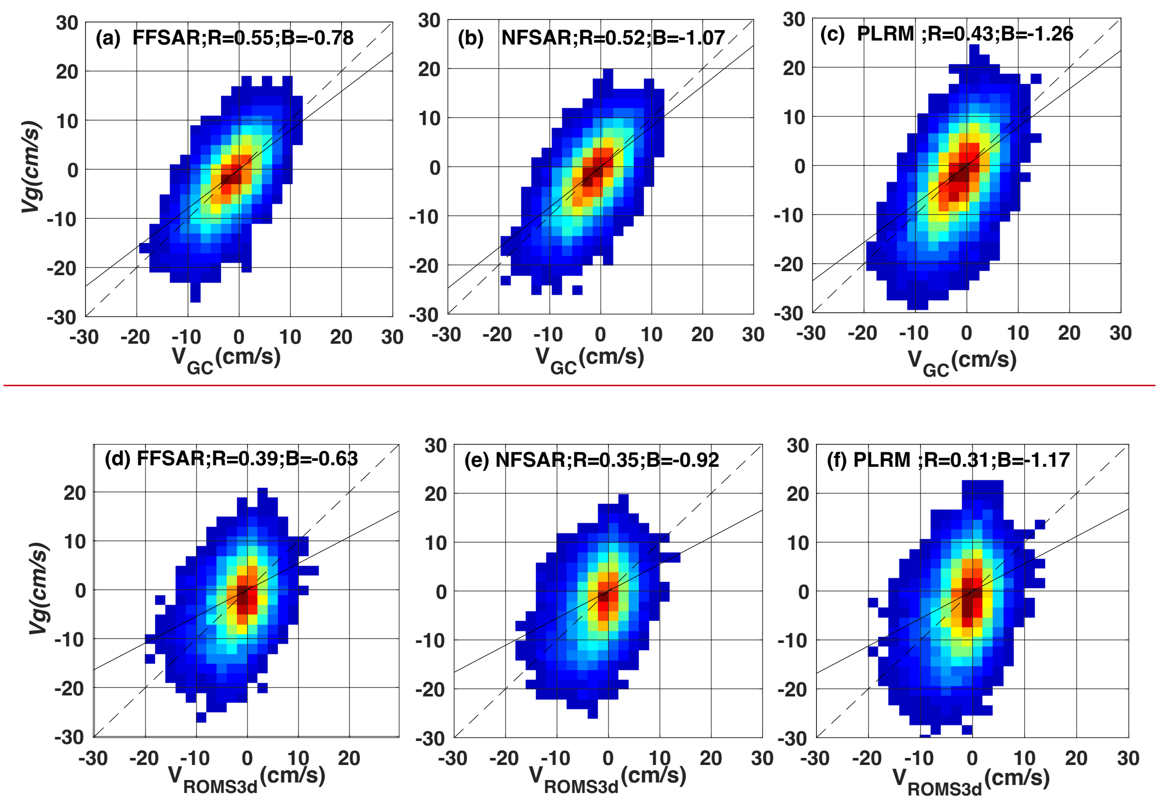

Fig. 5. (a) Time-latitude representation of cross-track absolute geostrophic current (*Vg*) estimated using FFSAR ADT=SSHA+MDT data as computed along S-3A repeat track 747, (b) the bathymetry along the track from offshore, over the shelf break and Georges Bank, across Georges Basin (GB), and then Jordan Basin (JB) to the eastern GoM coastline near 44.3N (see Figs. 1 and 8). FFSAR-based *Vg* is estimated using a 28km length scale. Note that negative *Vg* values indicate the southwestward current normal to the track, approximately along the local isobath on the coastal shelf. This pass crosses near two buoys I and M as labeled and shown with dashed black lines.

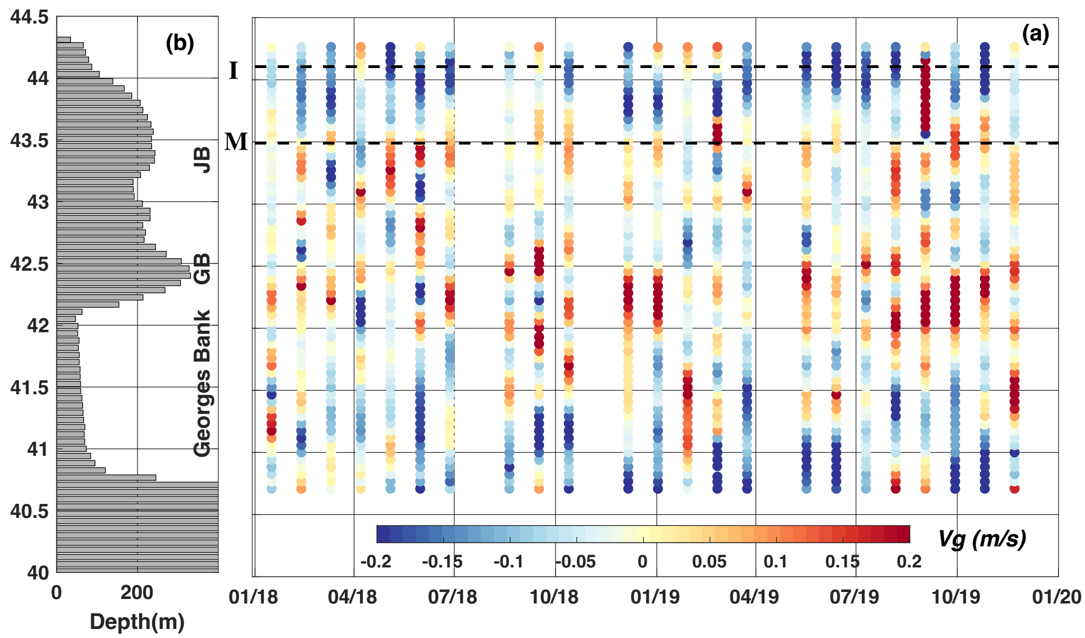

Fig. 6. (a) Match-up time series of S-3A cross-track absolute geostrophic current *Vg* derived from altimeter data products (FFSAR,UFSAR, and PLRM), and buoy measurements. $V_{Buoy(10\text{-}50m)}$ is the depth-integrated average current for 10-50m depths and V_{Buoy2m} is the surface current (see details in Section 3.3.2). (b) and (c) are scatter plots of altimeter *Vg* near S-3A track747 against $V_{Buoy(10\text{-}50m)}$ and V_{Buoy2m} from Buoy I in the GoM (Figs 5 and 8), respectively, with matchup sample number = 20, 18, and 17 for these *Vg* products FFSAR,UFSAR, and PLRM, respectively. *Vg* is estimated using a 14km length scale. All the correlation coefficients reported here are significant with $p<0.05$, excepting p~=0.06 for Vg_{PLRM} vs. $V_{Buoy(10\text{-}50m)}$.

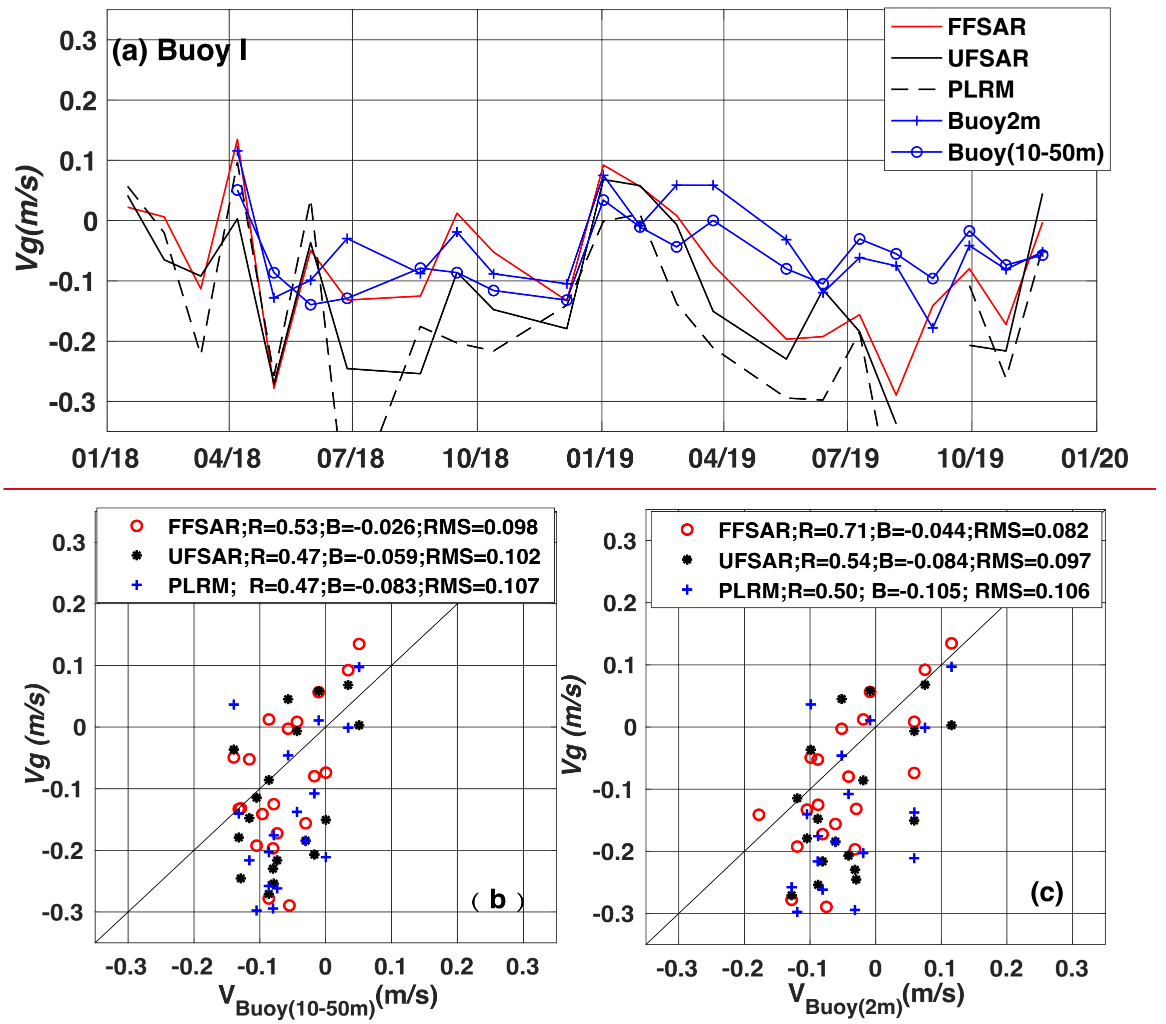

Fig. 7. The caption is the same as for Fig. 6, but now for Buoy M with a matchup sample number of 23 for the three *Vg* products. Buoy-measured $V_{Buoy(18\text{-}50m)}$ is the depth-integrated average in 18-50m. Altimeter *Vg* is estimated using a 28km length scale. The only correlation coefficients are statistically significant at p <0.01 and <0.03, respectively, for *Vg* FFSAR and *Vg* UFSAR vs. $V_{Buoy(18\text{-}50m)}$.

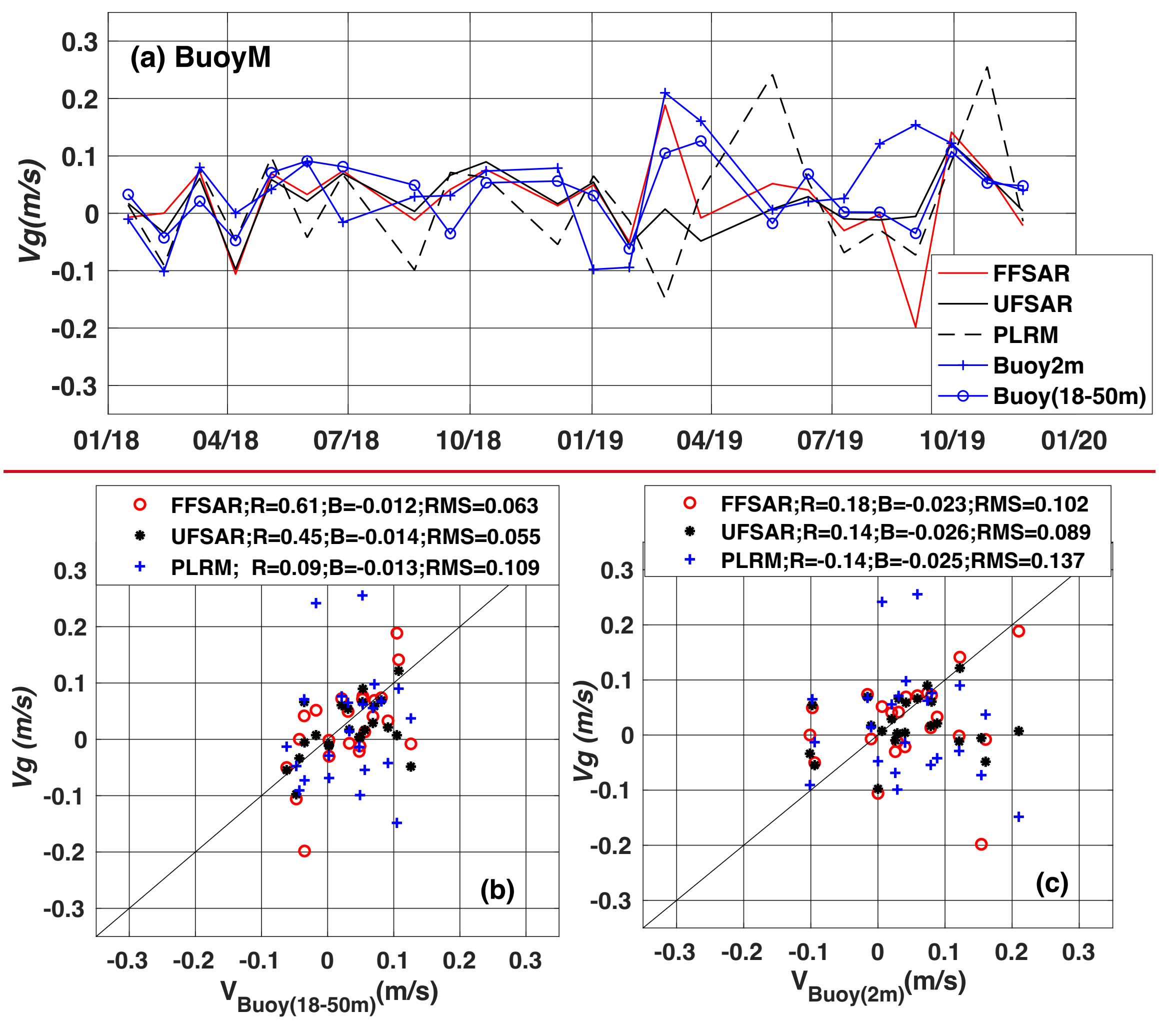

Fig. 8. Regional map including FFSAR cross-track absolute geostrophic current *Vg* using a 42km length scale, as well as red circles for buoys I (near 44N) and M (near 43.5N), along the four S-3A identified passes, T747 (27-Jun-2018) in the Gulf of Maine from the shelf break across the Georges Bank, Georges Basin, Jordan basin to the eastern GoM coast, T205 (8-Jun-2018) from the shelf break across Browns Bank, the North Channel and to the Cape Sable Shelf (CSS), T547 (24-May-2018) and T005 (1-Jun-2018) across the Scotian Shelf. This FFSAR-derived *Vg* mapping depicts the general along-shelf current in the early summer of 2018 (from May 24 to Jun 27, 2018).

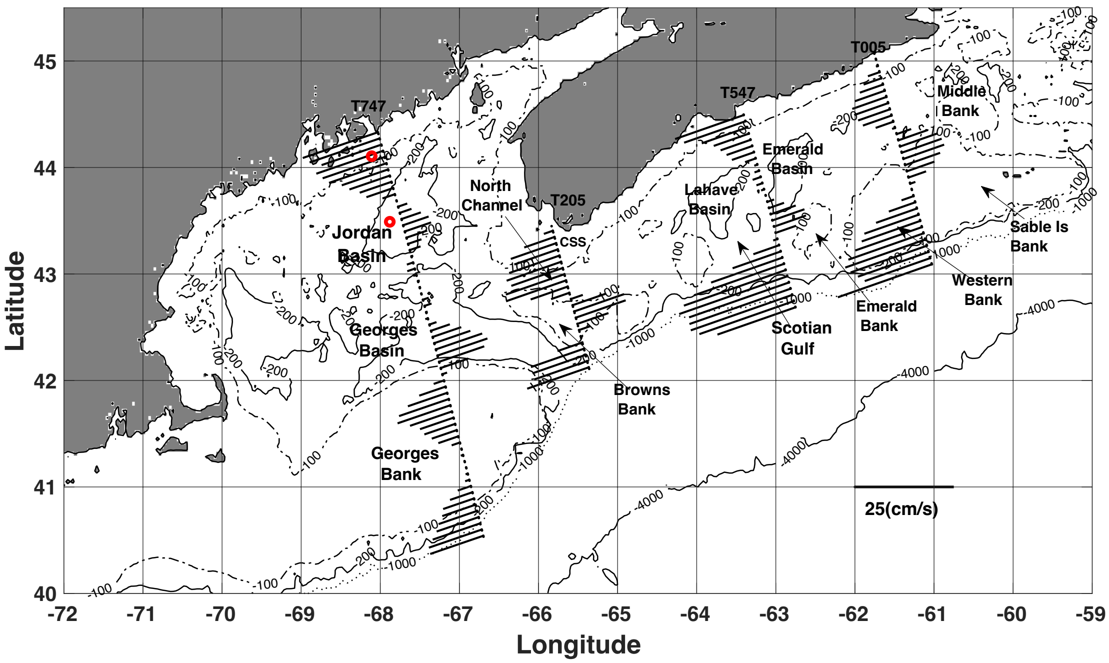

Fig. 9. Latitude vs. S3A-derived cross-track absolute geostrophic current *Vg* estimates using a 42km length scale, as well as reference currents along S-3A pass 747 (27-Jun-2018) in the Gulf of Maine (see Fig. 8). Panels (a) bathymetry, (b) Vg_{FFSAR}, (c) Vg_{UFSAR}, (d) Vg_{PLRM}, and (e) a set of current products, Vg_{FFSAR} and Vg_{PLRM} , as well as V_{GC} from GlobCurrent and V_{ROMS_3davg} from the 50m depth-averaged and 3-day running average from ROMS regional circulation model.

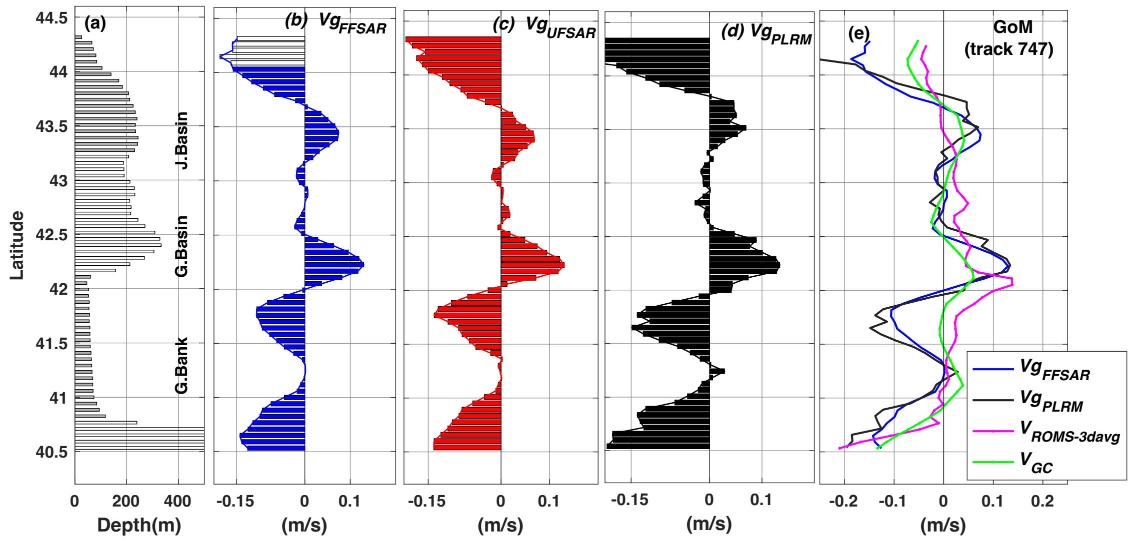

Fig. 10. Latitude vs. (a) bathymetry and (b) S-3A-derived cross-track absolute geostrophic current *Vg* estimates (using a 42km length scale) Vg_{FFSAR} and Vg_{PLRM} plus reference currents V_{GC} and V_{ROMS_3davg} along S-3A pass 205 (8-Jun-2018) from the shelf break across Browns Bank, the North channel (NC) and to the Cape Sable shelf (CSS) (see Fig. 8).

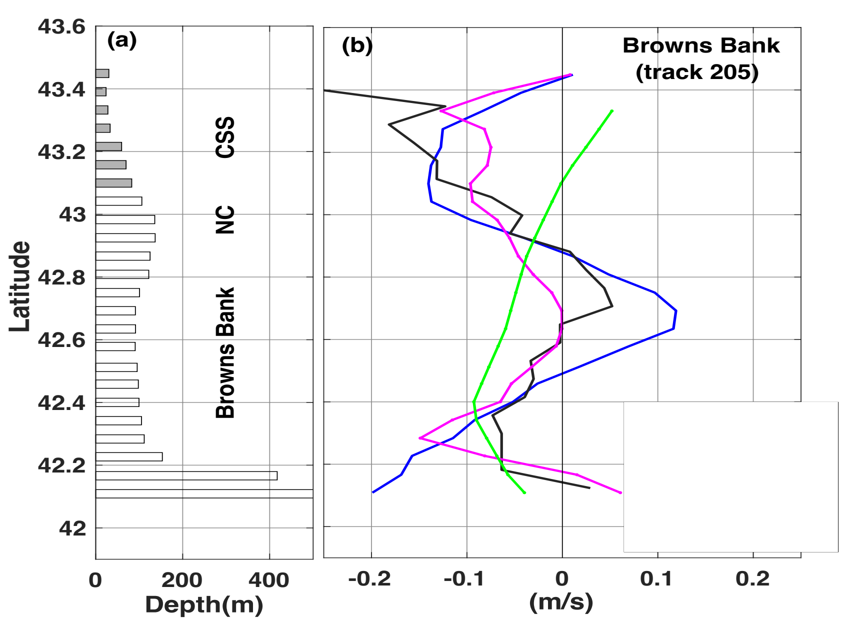

Fig. 11. The caption is the same as for Fig. 10, but now along S-3A pass 547 (24-May-2018) across the Nova Scotian Shelf (see Fig. 8).

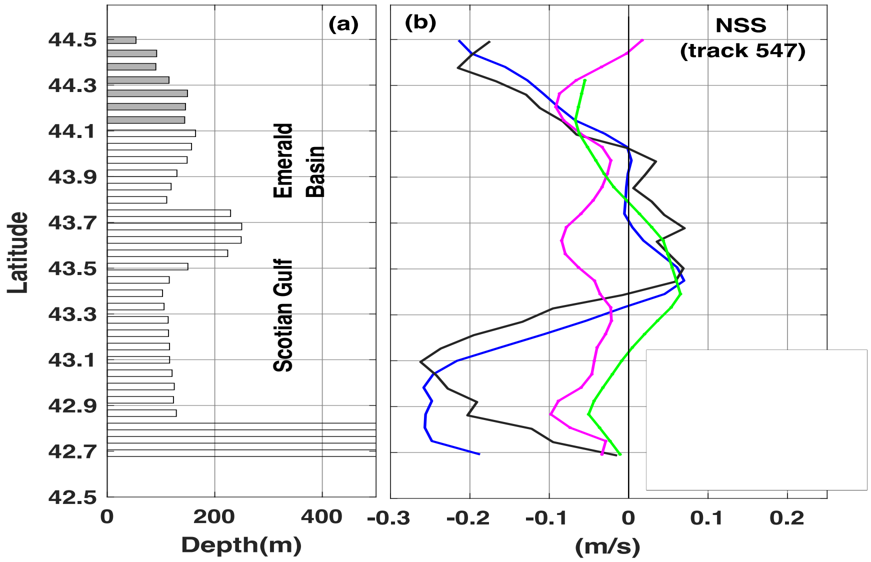

Fig.12. The caption is the same as for Fig. 10, but now along S-3A pass 005 (1-Jun-2018) across the Nova Scotian Shelf without ROMS data (this pass lies outside of the model domain) (see Fig. 1).